Investigating the role of deep weathering in critical zone evolution by reactive transport modeling of the geochemical composition of deep fracture water

Julien Ackerer, Coralie Ranchoux, Yann Lucas, Daniel Viville, Alain Clément, Bertrand Fritz, Catherine Lerouge, Gerhard Schafer, François Chabaux

Investigating the role of deep weathering in critical zone evolution by reactive transport modeling of the geochemical composition of deep fracture water

Ackerer J., Ranchoux C. , Lucas Y., Viville D., Clément A., Fritz B., Lerouge C., Schäfer G., Chabaux F.

Institut Terre et Environnement de Strasbourg, Université de Strasbourg, CNRS, ENGEES, 5 rue René Descartes, 67084 Strasbourg Cedex, France.

Abstract

Relatively little is known about the deep water circulation and the role of deep weathering processes on the Critical Zone (CZ) evolution. In this study, major fractures from four deep boreholes and water collected from these fractures (20-60 m of depth) were studied to improve our understanding of the deep CZ in a granitic headwater watershed (Strengbach watershed, France). Geochemical analysis indicates that chemical composition of deep water (20-60 m) is clearly different than shallow subsurface waters (0-15 m), with higher mean concentrations and a stronger spatial variability across the watershed. Reactive-transport modeling performed with the 1D KIRMAT code (KInetic of Reaction and MAss Transport) highlights the role of minor mineral dissolution (i.e. dolomite) and of longer mean transit time (100-597 yr) along fractures for explaining these differences. The obtained results also shed light on the difference of hydrogeochemical functioning between shallow subsurface system (water sampled from springs and piezometers) and deep system (deep water from borehole fractures). The shallow subsurface system (0-15 m) is characterized by a spatially relatively homogeneous water flow, high mean pore velocities, and water-rock interactions in a porous regolith, while the deep water circulation (20-60 m) behaves much more as independent systems along fractures, with low mean pore velocities, and variable mineralogy and hydrodynamic conditions. A state of chemical equilibrium can also be reached along fractures in the deep CZ for some primary minerals (biotite and K-feldspar), a feature never observed so far in the simulations of shallow subsurface water chemical composition in the Strengbach watershed. Even if the deep water exhibits higher solute concentrations, significantly lower mean pore velocities inferred in the fractured zones imply that the deep water is responsible for a very small part of the total hydrologic and weathering fluxes in the watershed. The limited role of the deep weathering processes (20-60 m) compared to the shallow subsurface

processes (0-15 m) suggests an up to bottom control of the CZ evolution at a millennial timescale. Our results also indicate that the majority of fresh water available for water supply at a human timescale originates from shallow subsurface waters, as the deep water circulation is too low for being critical at a timescale relevant for societal needs in this type of geological context.

1. Introduction

To improve our understanding of the critical zone (CZ), defined as the uppermost layer of Earth where rock, water, air, and life meet dynamically, is a key issue for predicting future soil and water resources (Bales et al., 2006; Brantley et al., 2007; Chorover et al., 2011). Most of the supply of fresh water to human activities depends on several meters of soil, saprolite, and fractured rock across the landscape (Gleeson et al., 2016). These different vertical compartments of the CZ have distinct physical, geochemical, and hydrologic properties. Water can flow vertically through soil, saprolite, and fractured bedrock, and laterally depending on the permeability architecture of the CZ (Brantley et al., 2017). Hydrologic processes have been studied in soils for decades, but much less is known about deep groundwater and its control on CZ evolution (Chabaux et al., 2017; Lucas et al., 2017). This gap of knowledge is primarily due to the challenges of sampling and gathering information from the base of the CZ shielded by many meters of weathered materials (Riebe et al., 2017; Holbrook et al., 2019).

Motivated by several scientific questions and societal needs, study of deep water circulation and associated weathering processes recently received more attention from the scientific community (e.g. West, 2012; Holbrook et al., 2014; Lucas et al., 2017; O'Geen et al., 2018). Rock moisture represents a water reserve that is distinct from soil moisture, and there is a growing recognition that rock moisture is an important but yet poorly understood component of the hydrological cycle (Salve et al., 2012; Dralle et al., 2018; Rempe and Dietrich, 2018). There is also an increasing demand for accurate estimates of water storage capacity and water transit time in watersheds, which are partially controlled by the diversity of flow paths, and central to predicting water availability in the environment (O'Geen et al., 2018; Weill et al.,

2019; Ackerer et al., 2020b). The role of groundwater storage on vegetation, plant rooting depth, and on the resilience of forest ecosystem to drought similarly encouraged the study of the deep water in the saprolite and in the fractured bedrock (Fan et al., 2017; Klos et al., 2018). Investigating the deep water circulation is equally important to evaluate the dominance of surface, shallow subsurface or deep water sources for rivers, which is necessary to understand the role of mixing processes in shaping concentration-discharge relations (C-Q relations; e.g. Kim et al., 2017; Liu et al., 2017; Zhi et al., 2019).

Among the recent advances, sampling of boreholes played a major role in improving our knowledge of the deep weathering processes and provided new opportunities to sample water from the deep CZ (e.g. Brantley et al., 2013; Buss et al., 2013; Chabaux et al., 2017; Hahm et al., 2019; Holbrook et al., 2019). Boreholes and deep cores allow for exploration of deep water chemistry (Chabaux et al., 2017; Ranchoux et al., 2021), mineralogical assemblages along fractures (Holbrook et al., 2019), and the role of deep water in water storage capacity (Hahm et al., 2019). These studies demonstrated that deep water chemistry can be distinct from surface or shallow subsurface water chemistry, and that fractures primarily control the water flow in the deep CZ. Reports also indicate that the mineralogy of fractures usually contrasts with the unweathered surrounding bedrock (protolith; Holbrook et al., 2019), implying specific water-rock interactions along fractures. Despite these recent advances, several questions remain open concerning the deep water circulation in the CZ. For example, to what extent is the hydrogeochemical functioning of the deep CZ different from the shallow subsurface system? What is the role of the deep water circulation in CZ evolution? How deep do models need to go to capture the hydrological and geochemical dynamics of a watershed?

A promising direction to explore these questions is the reactive transport modeling of the geochemical composition of deep water. Reactive transport models are a unique tool to evaluate in an integrative way the coupling between hydrologic and geochemical processes in the CZ (e.g. Moore et al., 2012; Salehikhoo and Li, 2015; Steefel et al., 2015; Heidari et al., 2017; Li et al., 2017; Ackerer et al., 2020a; 2020b). Reactive transport models were frequently applied in the context of fractured systems (MacQuarrie and Mayer, 2005; Yasuhara and Elsworthy, 2006; Deng and Spycher, 2019), with a specific focus on the modeling of fracture aperture change, the formation of an altered layer in the fracture region, or the physics of fluid flow in fractured media (Steefel and Lichtner, 1998; Meakin and Tartakovsky, 2009; Battiato et al., 2011; Deng et al., 2016). Reactive transport models provide a new opportunity to link the large variety of data collected from borehole campaigns, including deep water geochemistry, fracture mineralogy and fracture geometry.

However, only few studies have attempted to capture the geochemical composition of deep water with a reactive transport model (e.g. Lucas et al., 2017). Even rare are studies that estimate the mean transit time of deep water through reactive transport simulations and seek to quantify the spatial variability of deep water geochemistry at the watershed scale. These investigations are challenging, especially because they require an extensive hydrogeochemical database for several deep boreholes distributed across a single watershed. These data are available for the Strengbach watershed (figure 1), one of the reference headwater sites of the French critical zone network (OZCAR), where multidisciplinary studies have been conducted since 1986 (“Observatoire Hydrogéochimique de l’Environnement”, OHGE; El Gh’Mari, 1995; Fichter et al., 1998; Viville et al., 2012; Ackerer et al., 2016; 2020; Schmitt et al., 2017; Chabaux et al., 2017; 2019; Daval et al., 2018; Pierret et al., 2018). In this study, we aim to strengthen our understanding of weathering processes in the deep CZ with

134 the help of 1D reactive transport simulations capturing deep water geochemical composition
135 along major fractures in boreholes. More specifically, our study focused on the following
136 research questions: (1) What is the spatial variability of deep water geochemical composition
137 collected from several boreholes probing the deep CZ in an elementary watershed? (2) What
138 is the difference of hydrogeochemical functioning between the deep CZ and the shallow
139 subsurface? And (3) what is the significance of deep weathering processes in CZ evolution
140 compared to shallow subsurface weathering processes?

141 **2. Study site**

142 The Strengbach watershed is a small watershed (0.8 km²) located in the Vosges Mountains of
143 northeastern France at elevations between 883 and 1147 m (figures 1a and 1b). The climate
144 is mountainous oceanic, with an annual mean temperature of 7 °C and an annual mean rainfall
145 of approximately 1400 mm. 10 to 20% of the total precipitation is falling as snow during two
146 to four winter months. The annual mean evapotranspiration and runoff are of approximately
147 600 mm and 800 mm, respectively (Viville et al., 2012; Pierret et al., 2018). The vegetation is
148 currently dominated by beech and spruce forest. High-flow events in the Strengbach stream
149 occur at the end of winter season or in the early spring and drier conditions commonly happen
150 at the end of summer or during autumn. An updated overview of the Strengbach hydrologic
151 and climatic characteristics can be found in Pierret et al. (2018).

152 The bedrock is a base-poor Hercynian granite (-330 to -323 Ma; Schulmann et al., 2002),
153 fractured and hydrothermally overprinted, with a degree of hydrothermal alteration
154 decreasing from north to south (El Gh'Mari, 1995; Fichter et al., 1998). Fractures are primarily
155 present as a set of ~N30 fractures sub-parallel to the main fault zones around the Strengbach
156 watershed. The granite is mainly composed of quartz (35%), albite (31%), K-feldspar (22%)

157 and biotite (6%); it also contains small amounts of muscovite (3%), anorthite (2%), apatite
158 (0.5%) and clay minerals (0.5%; El Gh'Mari, 1995). During the Tertiary (-45 to -10 Ma), rifting
159 leading to the Rhine graben formation was associated to fluid circulations and formation of
160 secondary minerals as carbonates and clays in fractures (Dezayes and Lerouge, 2019). The
161 bedrock was also affected by meteoric weathering and glacial/periglacial processes during
162 the Quaternary (Ackerer et al., 2016), and the watershed's surface is currently covered by a
163 50 to 100 cm-thick acidic and coarse-in-texture soil (Hyperdystrict Cambisol). The saprolite
164 developed into the bedrock constitutes an aquifer from 1 to approximately 8 meters of
165 thickness with an average thickness of four meters. Saprolite is thinnest (1m) at the
166 watershed's crest and thickest (8-15m) near the stream (Weill et al., 2019; Ackerer et al.,
167 2020a).

168 An extensive database exists for the study of the CZ structure and its dynamic in the
169 watershed, including regolith profiles (Ackerer et al., 2016), soil solutions (Gangloff et al.,
170 2014; Prunier et al., 2015), shallow subsurface and spring waters (0-15 m of depth; Ackerer
171 et al., 2018), stream waters (Viville et al., 2012), and rock and water samples from deep
172 boreholes (20-60 m of depth; Chabaux et al., 2017).

173 **3. Database**

174 **3.1 Boreholes**

175 This study is based on data obtained from the hydrologic and geochemical monitoring carried
176 out in the Strengbach watershed since 1982. More specifically, the core of the study relies on
177 data from drilling campaigns undertaken since 2012 to investigate the deep CZ in the
178 watershed (Chabaux et al., 2017; Ranchoux, 2020; Ranchoux et al., 2021). Six boreholes were
179 drilled to study the bedrock properties, the mineralogy along fractures, and to collect the

deep water in the watershed bedrock. Borehole locations were selected strategically to sample two elevation profiles along the two main slopes of the watershed (figures 1b, 1c, 1d). F1a, F1b and F5 boreholes are located on the southern part and F6, F7 and F8 boreholes are located on the northern part of the watershed (figures 1c and 1d). All these boreholes cut across the soil (0-2 m), the saprolite (2-15 m) and the deep bedrock (15-120 m). Soil and saprolite thicknesses vary between boreholes and are in general thinner for boreholes nearby the watershed crests and thicker nearby the Strengbach stream. Drill cores were extracted from boreholes and stored at ITES (Institut Terre et Environnement de Strasbourg), formerly LHyGeS (Laboratoire d'Hydrologie et de Géochimie de Strasbourg), for further petrological, mineralogical, and geochemical analysis.

3.2 Fractures

The fracture network in the bedrock was constrained by geophysical mapping of boreholes, including optic scanner, acoustic scanner, and natural gamma ray measurements (Ranchoux, 2020; Ranchoux et al., 2021; illustration in figure 2a). For each fracture, depth, dip, azimuth, and aperture were measured. Fracture mineralogy was studied by macroscopic description, X-ray analysis, and thin section observation. X-ray analysis was performed at ITES and following the method presented in Ackerer et al., 2016. The mineralogical compositions of all powdered 250-µm bulk samples were determined with a Siemens D5000 diffractometer with scanning from 4 to 84°, a space step of 0.04° and a time step of 18 s. The <2-µm clay fractions were separated by centrifugation and analyzed after air drying and treatment with glycol ethylene and hydrazine to distinguish illites, smectites, kaolinites and inter-stratified clays. The quantitative estimation of the proportion of the different minerals was performed by the

Rietveld method with the Siroquant software (Ackerer et al., 2016). The analytical uncertainty was approximately 3 % for the mass fraction of primary minerals and 5 % for the mass fraction of clays.

Thin section observation was performed at BRGM ("Bureau des Recherches Géologiques et Minières", Orléans, France), including natural light, polarized light and cathodoluminescence images. Sampling was emphasized for major fractures in the deep CZ with a large aperture and showing evidence of deep water circulation, as the observation of weathered granite, granitic gruss, clay filling and/or trace of hydroxide minerals (an example of deep weathering evidence is shown in figure 2b). Mineralogical samples were collected on fracture planes to analyze weathered granite in contact with water. Few samples were also taken perpendicular to the fracture direction to analyze less weathered material and protolith. Major fractured zones were located at approximately 45 m of depth for F5, 63 m for F6, 42 m for F7 and 27 m for F8. These major fractured zones are named F5 45 m, F6 63 m, F7 42 m and F8 27 m, respectively. The geometry of fractures in these major fractured zones is reported in table 1 and mineral mass fractions and reactive surfaces are given in table 2.

All fractures contain the main silicate minerals found in the granite, as quartz, albite, anorthite, K-feldspar, muscovite, and biotite (figure 3). Thin section observation spotted few traces of weathering for quartz (figure 3a and 3c) and an increase of the weathering degree from K-feldspar to anorthite (figure 3a and 3d). Traces of hydroxide minerals and clay minerals were detected in the fractures, and clays were dominated by montmorillonites-smectites and illites (figure 3c). A modest variability of the abundance of the primary silicate minerals was observed for the major fractures (table 2). Thin section observation also showed carbonate minerals, mainly in the form of secondary dolomite precipitated during past hydrothermal

circulations in fracture fillings (figure 3b). Contrary to the silicate minerals, a high variability of the dolomite abundance was observed from one fracture to another, with the highest amount of dolomite in F6 at 63 m depth, intermediate amounts in F7 at 42 m and F5 at 45 m, and the lowest amount in F8 at 27 m (table 2). These data are supplemented by mineralogical analysis in soils and regolith from Ackerer et al., 2016.

3.3 Deep and shallow subsurface waters

Several sampling campaigns for deep water from boreholes were realized under different hydrologic conditions in the watershed (sampling dates in table 3). The deep water was sampled for each date in front of the major fractured zones F5 45 m, F6 63 m, F7 42 m and F8 27 m. For example, one sample was collected at 45 m depth in F5 borehole on May 5, 2015, merging the water delivered by the three fractures in this fractured zone (table 1). Pumping tests and in situ conductivity measurements were performed to confirm the inflow of deep water at these depths (Ranchoux, 2020). The geochemical composition of the deep water samples was determined at ITES for main cations (Na^+, K^+, Mg^{2+} and Ca^{2+}), main anions (Cl^-, NO_3^-, SO_4^{2-}), H_4SiO_4, pH and alkalinity following the analytical procedure classically used in the laboratory and detailed in Gangloff et al., 2014 and Lucas et al., 2017 (results in table 3). Hydrological and geochemical data were also available for the shallow subsurface water from previous studies conducted in the watershed (0-15 m of depth; stream, springs, and water collected in piezometers; Viville et al., 2012; Ackerer et al., 2018; 2020a).

4. Reactive transport modeling

4.1 Governing equations of reactive mass transport

Most coupled reactive transport models rely on the resolution of the partial differential equation in a saturated porous medium and that resulting from geochemical phenomena, added to the transport equation as a sink / source term (e.g. M'nassri et al., 2019). The classical hypotheses of instantaneous homogeneous reactions, of equal diffusion coefficients of all present aqueous species and only considered kinetics of heterogeneous reactions allows us to express the mass balance equation in terms of generalized concentrations Ψ_j (in mol per water mass or volume) of primary species. Under these conditions, the mass balance equation of reactive transport in a one-dimensional porous medium is written as (e.g., Lichtner, 1988; Gérard et al., 1998; M'nassri et al., 2019):

$$\frac{\partial}{\partial t}(\phi\Psi_j) = \phi D\left(\frac{\partial^2\Psi_j}{\partial x^2}\right) - v\frac{\partial\Psi_j}{\partial x} - \sum_{r=1}^{M}\alpha_{jr}\frac{\partial}{\partial t}(\phi_r\widetilde{V_r^{-1}}) \quad (j = 1, \dots., N), \qquad (1)$$

and

$$\frac{\partial}{\partial t}(\phi_r\widetilde{V_r^{-1}}) = v_r \quad (r = 1, \dots., M), \qquad (2)$$

where equation (1) refers to N aqueous primary species, and equation (2) to M primary species of reacting minerals. In these equations ϕ denotes the porosity of the porous medium, ϕ_r and α_{jr} denote the volume fraction and the stoichiometric reaction coefficients, respectively, of the r mineral with molar volume $\widetilde{V_r}$. v_r represents the reaction rates of the irreversible reaction of minerals and fluids equivalent to the rate of precipitation or dissolution of reacting minerals *r* per unit of the rock and fluid system (by convention, $v_r$is taken as positive for precipitation and as negative for dissolution reactions). D denotes the longitudinal hydrodynamic dispersion coefficient, and v denotes the Darcy velocity. Note that the mean velocity U is generally defined by $U = v/\phi$. The generalized concentration Ψ_j is defined according to the expression (M'nassri et al., 2019):

$$\Psi_j = C_j + \sum_i \alpha_{ji} C_i \quad , \text{with } \mathrm{C}_i = K_i \gamma_i^{-1} \prod_{j=1}^{N} \left(\gamma_j C_j\right)^{\alpha_{ji}} \quad (3)$$

where C_j refers to the concentration of the j primary species, and the sum runs over all aqueous secondary species with concentration C_i related to the concentrations of the primary species through the mass action equation. The quantity α_{ji} denotes the molar stoichiometric coefficient of species *j* in secondary species *i*, γ are the activity coefficient of the aqueous species, and K_i denotes the equilibrium constant. From (1) and (2) one obtains a system of N + M coupled nonlinear partial differential equations.

4.2 The reactive transport model KIRMAT

The simulations of the water chemical composition along the fractures were performed with the reactive transport KIRMAT code (KInetic of Reaction and MAss Transport; Gérard et al., 1998; Lucas et al., 2017; 2020; Ngo et al., 2014). KIRMAT is a thermokinetic model derived from the Transition State Theory (TST) that simultaneously solves the equations describing transport mass balance and geochemical reactions along a 1D direction. The mass transport comprises the effects of one-dimensional advection, diffusion, and kinematic dispersion. Chemical reactions consider the dissolution of primary minerals and oxido-reduction reactions, in addition to the precipitation of secondary minerals and clay minerals. In KIRMAT, the water-rock interactions involve dissolution and precipitation processes (see eq. 2), which are controlled by many factors including the mineral reactive surface, the aqueous solution composition (ion activities), the temperature, and the degree of saturation of the aqueous solution with respect to the studied mineral.

The workflow in KIRMAT is organized in three steps (M'nassri et al., 2019). In the first step, the ionic speciation (initial equilibrium) and the saturation index are calculated. During the

second step the perturbation of this initial partial equilibrium state by irreversible water-rock interactions due to dissolution or precipitation of minerals (reaction term v_r, see eq. 2), resulting in either supplying or removing elements from the aqueous solution, is modeled. Then, finally, the (N+M) partial differential equations (1) and (2) are solved simultaneously with a one-step algorithm. The mass transport equations are solved using the finite difference approximation in an explicit scheme.

4.3 Water-rock interactions in KIRMAT

In KIRMAT, the kinetic of primary mineral dissolution v_r (in mol per water mass) is quantified by (Ngo et al., 2014):

$$v_r = \mathrm{k_{d,r}} \mathrm{S_r^{eff}} \alpha_{\mathrm{H^+}}^{\mathrm{n}} \left[1 - \left(\frac{\mathrm{Q_r}}{\mathrm{K_r}}\right)^{\mathrm{n1}}\right]^{\mathrm{n2}} \quad (4)$$

where $\mathrm{k_{d,r}}$ is the kinetic rate constant of dissolution (mol m^{-2} yr^{-1}) of the reactive mineral r, $\mathrm{S_r^{eff}}$ the reactive surface area of the reactive mineral r (m^2 Kg^{-1} H_2O), $\alpha_{\mathrm{H^+}}^{\mathrm{n}}$ the activity of proton, $\mathrm{Q_r}$ the ion activity product of the reactive mineral r, $\mathrm{K_r}$ the thermodynamic equilibrium constant of the hydrolysis reaction of the reactive mineral r, and n1 and n2 the exponents depending on the pH of the water (M'nassri et al., 2019; Lucas et al., 2020). Oxido-reduction reactions are described through Nerst equations, and the precipitation rate v_r of a secondary mineral other than clay minerals (ex: calcite, goethite) is described by the expression:

$$v_r = \mathrm{k_{p,r}} \mathrm{S_r^{eff}} \left[\left(\frac{\mathrm{Q_r}}{\mathrm{K_r}}\right)^{\mathrm{p}} - 1\right]^{\mathrm{q}} \quad (5)$$

with $k_{p,r}$ the kinetic rate constant of precipitation (mol m^{-2} yr^{-1}) of the reactive mineral r, and p and q the exponents describing the dependence of the reaction from the saturation state (Ngo et al., 2014). The saturation index (SI) of the reactions occurring between the aqueous species and minerals is defined by:

$$SI_i = log \frac{Q_i}{K_i} \quad (6)$$

where Q_i denotes the ion activity product and K_i denotes the thermodynamic equilibrium constant. If the water sample is completely saturated with the dissolved mineral, SI equals to zero. Positive values of SI indicate super-saturation and the mineral would tend to precipitate; negative ones indicate under-saturation and the mineral would tend to dissolve. For each species and minerals in the studied system, the equilibrium constants are obtained by applying the corresponding activity coefficients. The formation of clay minerals is handled with a clay solid solution in KIRMAT. The clay fraction is defined as a solid solution made up of a combination of pure clay end-members. The ion activity product Q_i of the pure clay end member i is expressed by:

$$Q_i = K_i X_i \gamma_i \quad (7)$$

with K_i the thermodynamic equilibrium constant of the hydrolysis reaction of the clay end member i, X_i the molar fraction of the clay end member i in the solid solution, and γ_i the activity coefficient of the clay end member i. The clay solid solution is precipitated at thermodynamic equilibrium and its chemical composition varies over time, depending on the evolution of the water chemistry and the rock mineralogy. This multicomponent solid solution aims to imitate the impurity of clay minerals precipitated during low-temperature water-rock interactions typical of chemical weathering reactions (Tardy and Fritz, 1981).

4.4 Modeling strategy

The strategy to capture the geochemical composition of deep water was adapted from previous modeling studies conducted in granitic headwater watersheds (Strengbach and Ringelbach watersheds; Lucas et al., 2017; Ackerer et al., 2018; 2020a). In contrast to shallow subsurface flow (0-15 m), which is localized in the soil or in the saprolite, deep water flow observed in boreholes is controlled by the major fractures existing in the granitic bedrock (Lucas et al., 2017). The reactive transport modeling was therefore adapted to consider water-rock interactions occurring along fractures (figure 4).

Starting point was the choice of the input soil solution used for the modeling (figure 4a). The soil solutions from the beech site (HP-70, Prunier et al., 2015), collected at 70 cm of depth on the southern slope (figure 1b), were assumed to be representative of the input concentrations of aqueous species percolating into the granitic bedrock for F5 45 m (F5 borehole located on the southern slope, figure 1b). The soil solutions from the spruce site (VP-60, Prunier et al., 2015), collected at 60 cm of depth on the northern slope (figure 1b), were assumed to be representative of the initial input solution for F6 63 m, F7 42 m and F8 27 m (F6, F7 and F8 boreholes located on the northern slope, figure 1b). This choice assumes that the deep water circulation is most likely supplied by infiltrations of water from the upper regolith. The chosen modeling approach is based on the main assumption that soil solutions recharge fractures only at the top of the watershed and then react along fractures. Soil solutions do not enter along fractures at greater depth, which is supported by the absence of weathering signs in the protolith surrounding fractures.

For each borehole, the deep water flow was assumed to occur along the main fractures identified by the borehole imaging (table 1). The fracture was modeled as a 1D stream tube following the direction of the local slope, with a length equal to the distance between the fractured zone in the borehole and the top of the corresponding hillside (figure 4a). The stream tube was discretized with a spacing of 1m long meshes. This modeling scheme did not consider the tortuosity of the fracture network, which was largely unknown, and assumed that all the fractures were extending along a simple line following the local slope. The aperture known from the borehole imaging (table 1) was supposed constant along the fracture and extended to the whole length along the hillslope (figure 4a).

In the case of a fractured zone with a single fracture intersecting a borehole (which is the case of F8, fractured zone at 27 m depth), only one simulation for each sampling date was performed to capture the water-rock interactions and the geochemical composition of deep water along the fracture. When several fractures are present in a fractured zone (for example F5 45 m, see figure 4b, F6 63 m, F7 42 m), independent simulations were performed for each sampling date and for each fracture, and the arithmetic mean of solute concentrations simulated for all fractures was calculated to quantify the mean chemical composition of the water in the fractured zone. Mean pore velocities along the fractures were adjusted to obtain the best agreement between modeled and measured concentrations in the fractured zones (F5 45 m, F6 63 m, F7 42 m, and F8 27 m), as the mean pore velocities in the deep fracture network are unknown. By combining the mean pore velocities and the fracture lengths, the optimized mean transit time of water was calculated along each fracture. Optimized mean transit times are therefore dependent on fracture geometry, flow velocity, mineralogical composition and mineral reactive surfaces in fractures.

A simple planar geometry was assumed for all the fracture surfaces to calculate the contact surface area between the water and the fracture rock (illustration in figure 4b, values of specific surface of water-rock contact in table 1). The reactive surfaces of minerals were determined by assuming that the surface area proportions of minerals along a fracture are identical to the mass fractions of minerals in the bulk samples of the fracture rock. For each fracture, the initial mineralogy used in the reactive transport modeling was adapted and constrained by the mineralogical composition of weathered granite along fracture planes (table 2). During simulations, the mineralogy evolves through time and varies spatially along fractures depending on water-rock interactions as primary mineral dissolution and clays precipitation. Thermodynamic and kinetic data for all the primary and secondary minerals are available in Ackerer et al., 2020a and in the supplementary material (tables EA1 and EA2). All the simulations were performed at the temperature of 7 °C, a temperature corresponding to the mean annual temperature measured in the borehole waters.

For the clay solid solution, clay end-members were defined on the basis of X-ray diffraction analyses and thin section observation of clay minerals present in fractures (figure 3). Clay end-members consist of K-Illites, Mg-Illites, Ca-Illites, Montmorillonites, Na-Montmorillonites, K-Montmorillonites, Ca-Montmorillonites and Mg-Montmorillonites, similarly to the clay end-members used in the simulation of the shallow subsurface water chemistry (Ackerer et al., 2020a). Chemical compositions and thermodynamic data for clay end members are available in Ackerer et al., 2020a and in the supplementary material (table EA3).

5. Results: geochemical water composition

On the basis of pH and alkalinity measurements, two groups of water are identified in the watershed: shallow subsurface water collected from 2 to 10 m depth (CS1 spring, PZ3, PZ5,

PZ7 piezometers) and deep water sampled in boreholes from 27 to 63 m (F5 45 m, F6 63 m, F7 42 m, and F8 27 m; figure 5a). Spring water and water from piezometers collected within the shallow subsurface show acidic pH (pH < 7) and low alkalinity (alkalinity < 0.1 meq/L). In contrast, deep borehole water shows slightly basic pH (7.5 < pH < 8.2) and much higher alkalinity (1 meq/L < alkalinity). Alkalinity and pH gradually increase from F7 42 m, F8 27 m, F5 45 m to F6 63 m (figure 5a).

Overall, solute concentrations of basic cations (K^+, Ca^{2+}, Mg^{2+} and Na^+) and dissolved silica (H_4SiO_4) are lower in the shallow subsurface water compared to the deep water (figures 5b, 5c and 5d). Solute concentrations are relatively homogeneous in the shallow subsurface system for spring and piezometer waters, especially for Ca^{2+}, Mg^{2+} and Na^+ concentrations (figures 5b and 5c). For Ca^{2+} and Mg^{2+}, the shallow subsurface water exhibits much lower concentrations compared to the deep water, while for H_4SiO_4, the trend in solute concentrations is more continuous between shallow and deep waters (figure 5d).

The geochemical water composition also indicates that for the deep water, there is not a single geochemical signature at the watershed scale, and each borehole has a deep water with a distinctive chemical composition. The variability of water chemical composition between boreholes is higher for Na^+, Ca^{2+} and Mg^{2+}, but relatively lower for K^+ and H_4SiO_4 (figures 5b, 5c and 5d, not shown for K^+). The water sampled from F6 63 m has the particularity to show highest Ca^{2+} and Mg^{2+} concentrations, but the lowest Na^+ and H_4SiO_4 concentrations. In contrast, the water sampled from F8 27 m has the highest Na^+, K^+ and H_4SiO_4 concentrations, but lower Ca^{2+} and Mg^{2+} concentrations. Water samples collected from F7 42m and F5 45m show most of the time intermediate concentrations in basic cations and dissolved silica and their concentrations are framed by F6 63 m and F8 27 m.

To identify the stable minerals under thermodynamic conditions encountered in the deep water, stability diagrams (also called activity diagram, e.g. Maher et al., 2011) were drawn to visualize the stability domains of several common minerals (figure 6). The chemical composition of all the deep water samples falls in the stability zone of montmorillonites, as exemplified in stability diagrams (figures 6a and 6b). The precipitation of other clay minerals (kaolinite, pyrophyllite) and of secondary minerals as hydroxides (gibbsite) is not favored under the given thermodynamic conditions. The instability of anorthite indicates that primary silicate minerals may experience dissolution even in the deep part of the CZ (figure 6a). Overly, the obtained stability diagrams indicate that at the first order, the weathering processes taking place in the deep water tend to dissolve primary minerals (ex: anorthite) and to precipitate clay minerals of the type of montmorillonites.

6. Results: reactive transport modeling

The chemical composition of the deep water is controlled by both the mineralogy and the hydrodynamic conditions along the fractures. Reactive transport modeling allows to understand the variability of geochemical water composition across boreholes and to link hydrodynamic conditions, water transit time, mineralogy, and solute concentrations.

6.1 Hydrodynamic conditions and mean transit time

The fracture lengths determined by taking the distance between the four fractured zones and the appropriate hillcrests are 700 m, 100 m, 350 m, and 400 m for F5 45 m, F6 63 m, F7 42 m and F8 27 m, respectively (table 4). The best agreement between measured and simulated solute concentrations are obtained with the mean pore velocities of 3.33 m yr^{-1}, 1 m yr^{-1}, 2.33 m yr^{-1}, and 0.67 m yr^{-1} for F5 45 m, F6 63 m, F7 42 m and F8 27 m, respectively (mean Kling-Gupta efficiency of 0.85, optimized parameters in table 4). By combining the mean pore

446 velocities and the fracture lengths it is possible to calculate the mean transit time of the deep
447 water in the deep CZ. Results point to a general increase of the deep water transit time from
448 F6, F7, F5 and F8 boreholes, which is compatible with deep water flowing from the top to the
449 bottom of the hillslope (table 4). The shortest mean transit time is determined for F6 63 m
450 (100 yrs) located near the top of the crest line in the northern part of the watershed (figure
451 1). Longer transit times are calculated for F7 42m and F5 45m (150 – 210 yrs) located at
452 intermediate elevations, and the longest transit time is determined for F8 27 m (597 yrs)
453 located near the Strengbach stream at the bottom of the northern slope (figure 1).

454 **6.2 Water-rock interactions and mineralogy**

455 Patterns of primary mineral saturation states in current weathering conditions are similar for
456 all the boreholes and results are shown in the following for the fractured zone F5 45 m (figure
457 7a). The calculated saturation states of primary minerals indicate that anorthite, apatite,
458 albite and dolomite are systematically undersaturated along the fractures ($\log(Q/K) < 0$; figure
459 7a). K-feldspar is slightly undersaturated at the beginning of the flow path but reaches a state
460 of chemical equilibrium after approximately 100 years at the middle of the flow path ($\log(Q/K)$
461 $= 0$; figure 7a). Biotite and quartz are oversaturated along the whole flow path ($\log(Q/K) > 0$;
462 figure 7a).

463 Patterns of primary mineral dissolution rates are more variable between boreholes due to
464 the difference of mineral reactive surfaces in the fractured zones. This difference is controlled
465 by the mineralogical variability (mineral mass fractions in the fractured zones, table 2) and
466 the variability of fracture geometry (specific surface of water-rock contact, table 1). In
467 general, the highest dissolution rate is simulated for the dolomite (1.5×10^{-6} mol.yr^{-1}.kg H_2O^{-1}),
468 followed by the dissolution rates of albite and anorthite (1×10^{-6} and 7×10^{-7} mol.yr^{-1}.kg H_2O^{-1},

illustration for F5 45 m in figure 7b). The dissolution rate of dolomite tends to decrease along the flow path while dissolution rates of albite and anorthite remain stable (figure 7b). Apatite and K-feldspar show lower dissolution rates (5×10^{-8} and 1×10^{-7} mol.yr^{-1}.kg H_2O^{-1}), with the dissolution rate of K-feldspar decreasing before reaching a zero value approximately after 100 years at the middle of the flow path. The dissolution of biotite and quartz does not take place because of the oversaturated state of these minerals. This general pattern illustrated with the fractured zone F5 45 m is modulated by the difference of primary mineral reactive surfaces for the other boreholes. Higher reactive surfaces enhance higher dissolution rates, with for example higher dissolution rate of dolomite in F6 63 m due to the higher amount of dolomite in this fractured zone.

Precipitation rate and chemical composition of clay minerals precipitated during the simulations are similar for all the boreholes. A low precipitation rate of a clay solid solution is simulated all along the flow path in the fractured zones and its composition is made up of montmorillonites, in accordance with their thermodynamic stability in the deep water (figure 6). The chemical composition of the clay solid solution becomes stable after approximately 50 yrs (illustration for F5 45 m in figure 7d). The clay solid solution primarily constitutes of Ca-montmorillonite and Mg-montmorillonite (mass fractions of 42 % and 43 %, respectively), and secondarily of Na-montmorillonite and K-montmorillonite (mass fractions of 8 % and 7 %, respectively; illustration for F5 45 m in figure 7d).

6.3 C-MTT slopes and solute concentrations

The dynamic behavior of primary mineral dissolution and of clay mineral precipitation has a strong impact on the relationship between solute concentrations and mean transit time of deep water. The sensitivity of a solute concentration to an increase of the mean transit time

492 along the fractures can be quantified with the Concentration-Mean Transit Time slopes (C-
493 MTT slopes, Ackerer et al., 2020a). C-MTT slopes are controlled by the competition between
494 primary mineral dissolution and element incorporation into clay minerals along the flow path.
495 When elemental fluxes from primary mineral dissolution to solution are much higher than
496 fluxes from solution to clay minerals, the element can accumulate in solution, resulting in a
497 strong C-MTT slope. By contrast, when elemental fluxes from primary mineral dissolution to
498 solution are only slightly higher than fluxes from solution to clay minerals, the element
499 accumulates only slowly in solution, resulting in a weak C-MTT slope (Ackerer et al., 2020a).

500 Ca^{2+} is the basic cation with the highest C-MTT slope in the deep water system because Ca^{2+}
501 concentrations rapidly increase along the fractures due to the fast dissolution rates of several
502 Ca-bearing minerals as dolomite, anorthite, and apatite (illustration for F5 45 m in figure 7c).
503 Mg^{2+} also shows a relatively strong C-MTT slope due to the fast dissolution of dolomite in the
504 fracture network (figure 7c). Because Na^{+} in solution is only provided by the dissolution of a
505 single primary mineral with a lower dissolution rate (i.e. albite), the C-MTT slope of Na^{+} is
506 intermediate. H_4SiO_4 in solution is provided by the dissolution of many primary minerals
507 (albite, anorthite, K-feldspar, …), however, the precipitation of clay minerals also transfers Si
508 from water to the clay mineral structures, resulting in an intermediate C-MTT slope for H_4SiO_4.
509 K^{+} is the basic cation with the lowest C-MTT slope because K^{+} in solution is only provided by
510 the slow dissolution of K-feldspar (figure 7c). The K-feldspar also reaches a state of chemical
511 equilibrium along the flow path (figure 7a), which limits the increase of K^{+} concentrations in
512 the deep water. Elements with stronger C-MTT slopes (e.g. Ca^{2+}, Na^{+}) are therefore more
513 suitable as indicators of mean transit time than others with lower C-MTT slope because their
514 solute concentrations do not reach a plateau (figure 7c).

As for the mineral dissolution rates, C-MTT slopes are therefore impacted by the mineralogical variability and the difference of mineral reactive surfaces between fractured zones. By consequence, the evolution of the simulated chemical composition of the deep water is specific along each fractured zone, as exemplified by the different chemical trends in H_4SiO_4 - Na^+, Ca^{2+} - Na^+ and Mg^{2+} - Na^+ elementary diagrams (figure 8). Higher amounts and higher reactive surfaces of dolomite in F6 63 m (table 2, figure 3b) promote a rapid increase of Ca^{2+} and Mg^{2+} concentrations compared to Na^+ concentrations (figures 8b and 8c). Lower amounts and lower reactive surfaces of dolomite in F8 27 m imply a slow increase of Ca^{2+} and Mg^{2+} concentrations compared to Na^+ concentrations (figures 8b and 8c). F5 45 m and F7 42 m show intermediate trends in Ca^{2+} - Na^+ and Mg^{2+} - Na^+ diagrams. In the H_4SiO_4 - Na^+ diagram, F6 63 m and F7 42 m show a similar trend, while F5 45 m and F8 27 m show a parallel trend shifted by the difference of chemical composition of the initial input soil solution (figure 8a). These trends are explained by the competition between albite dissolution, the dissolution of the other silicate minerals, and the precipitation of clay minerals.

The final solute concentrations generated by the reactive transport model in the deep water of the fractured zones depend on both the C-MTT slopes and the mean transit time along fractures. Simulations capture the mean chemical composition in basic cations and in dissolved silica in the deep water of the fractured zones of all boreholes (figures 9). The low Na^+ and H_4SiO_4 concentrations in F6 63 m are primarily explained by the short mean transit time at F6 (figure 9a and 9b). The higher Ca^{2+} and Mg^{2+} concentrations are controlled by the strong C-MTT slopes for these elements in the fracture network of F6, implying a fast increase of these elements in solution (figure 9c and 9e). F8 27 m follows the opposite trend with a

538 longer mean transit time enhancing higher Na^+ and H_4SiO_4 concentrations (figure 9a and 9b).
539 Lower C-MTT slopes for Ca^{2+} and Mg^{2+} elements are explaining lower concentrations at F8
540 (figure 9c and 9e). F5 45 m and F7 42 m have intermediate C-MTT slopes and mean transit
541 time, resulting in intermediate concentrations (figure 9). K^+ concentrations are less variable
542 between the four boreholes due to the state of chemical equilibrium of K-feldspar along the
543 fractures, which reduces the difference of K^+ concentrations between boreholes (figure 9d).
544 The pH of water is slightly higher in the fractured zones with higher reactive surfaces of
545 dolomite (figure 9f).

546 **7. Discussion**

547 **7.1 Modeling scheme and uncertainties**

548 Results from reactive transport simulations are strongly dependent on the modeling scheme
549 assuming that deep water circulates along 1D independent fractures where minerals are only
550 exposed along a planar fracture surface. In our simulations, the flow velocity was adjusted
551 until the simulated water chemical composition matched the chemistry of sampled water
552 from boreholes (section 4.4). With the choice to model mineral surfaces as only in contact
553 with water along the fracture aperture and planar, the model generates slow weathering
554 reactions, which in turn relates to long residence times of deep water. Several additional
555 simulations were performed to evaluate the relevance of the modeling scheme and to provide
556 an estimation of uncertainties on reactive surfaces and mean transit times.

557 A way to evaluate if a planar geometry is realistic is to consider simulations in which reactive
558 surfaces along fractures are set equal to reactive surfaces from the shallow subsurface, as if
559 fractures were completely filled with a porous regolith. Reactive surfaces in the shallow
560 subsurface were calculated using a spherical geometry and assuming a porous and
561 homogeneous regolith (Ackerer et al., 2018; 2020a). Their values were able to capture the

562 geochemical composition of spring and piezometer waters and to reconcile hydrological and
563 geochemical modeling without modifying kinetic constants or rising a field-laboratory
564 discrepancy of kinetic rates. Simulations with shallow subsurface reactive surfaces thus
565 consider the fastest reaction rates given the background of hydrogeochemical modeling in
566 the watershed. Following the same modeling method detailed in section 4.4, flow velocity
567 along fractures was then adjusted to try to match deep water chemical composition.
568 However, whatever the flow velocity used in our simulations, it was not possible to capture
569 deep water chemistry with shallow subsurface reactive surfaces. One important particularity
570 of the deep water chemistry that could not be captured with shallow subsurface reactive
571 surfaces was the very high Ca^{2+} and Mg^{2+} concentrations contrasting with moderate Na^{+} and
572 H_4SiO_4 concentrations. This pattern is explained by dolomite dissolution. In a granitic setting,
573 dolomite cannot be present in the porous matrix of the bedrock, it is only present as
574 secondary mineral on fracture surfaces. This is why a planar geometry with minerals assign
575 on fracture planes is more realistic than a geometry with fractures filled with a porous
576 medium and high reactive surfaces.

577 The chemical contrast between deep water samples collected from different boreholes also
578 supports our modeling scheme based on independent fractures. Both major element
579 concentrations (this study) and isotopic compositions (U, Sr; Ranchoux et al., 2021) are
580 contrasted between boreholes, even while considering boreholes located on the same
581 hillslope. A highly fractured zone behaving like a porous medium or well connected fractures
582 would homogenize solute concentrations between boreholes located on the same hillslope
583 (F6, F7, F8). This is not the case, and the unique geochemical signature of each borehole
584 supports the view of discrete independent fractures. All of these points explain why a

585 modeling scheme based on discrete independent fractures with water-rock interactions
586 occurring along a planar geometry is a reasonable modeling approach.

587 Another way to constrain the discussion about reactive surfaces and mean transit time is to
588 compare the mean transit time of deep water inferred from the reactive-transport modeling
589 with independent age estimates obtained from other geochemical tracers. In parallel with
590 this study, CFCs (chlorofluorocarbons) concentrations were measured and modeled for deep
591 water from the main boreholes in the Strengbach watershed (Ranchoux et al., 2021). Deep
592 water ages inferred from CFCs data range between 50 and 200 years. The mean transit time
593 of deep water inferred from the reactive-transport modeling, between 100 and 600 years,
594 falls in the same order of magnitude of CFCs estimates (50-200 years). This underlines that
595 mineral reactive surfaces used in the modeling with a planar geometry are within a realistic
596 order of magnitude, otherwise a strong discrepancy would rise between numerically
597 calculated mean transit times and CFCs water ages. To estimate a plausible range of reactive
598 surfaces, we performed several additional simulations with higher reactive surfaces (initial
599 reactive surfaces multiplied by a factor of 2, of 5 and of 10). In accordance with the modeling
600 strategy detailed in section 4.4, the mean pore velocity was adjusted to match the chemical
601 composition of deep water and the optimized mean transit time was calculated for each
602 borehole. Simulations with reactive surfaces multiplied by a factor 2 and 5 cannot be
603 discarded as they render the water chemistry with mean transit times also compatible with
604 CFCs estimates. The mean transit times calculated in simulations with reactive surfaces
605 multiplied by a factor of 5 are near the lowest estimates of water ages determined from CFCs
606 (for example, in the case of F5 borehole, the optimized mean transit time is 42 years for the
607 5 times increased reactive surface, while the range of ages inferred from CFCs is between 61
608 and 124 years). Simulations with reactive surfaces multiplied by a factor of 10 and any

609 simulations with higher reactive surfaces produce too young waters for being compatible with
610 CFCs estimates. Therefore, a reasonable maximum uncertainty on reactive surfaces, flow
611 velocity and mean transit time is around a factor of 5.

612

613 **7.2 Hydrogeochemical functioning of the deep CZ compared to the shallow subsurface**

614 Our results clearly show that the deep water chemistry is very distinctive from the shallow
615 subsurface water chemistry monitored by previous studies conducted in the Strengbach
616 watershed (Viville et al., 2012; Prunier et al., 2015; Chabaux et al., 2017; 2019; Ackerer et al.,
617 2018; 2020a). The difference of hydrogeochemical functioning between the shallow
618 subsurface and the deep CZ can be explained in detail with the reactive transport model
619 developed in our study.

620 From the hydrologic point of view, the shallow subsurface flow (0-15 m) is a relatively
621 homogeneous flow in the porous regolith (Ackerer et al., 2020a), while the deep water flow
622 (20-60 m) is much more localized along the major fractured zones in the bedrock (Lucas et al.,
623 2017; Ranchoux, 2020). This difference in hydrologic functioning promotes a modest spatial
624 variability of the shallow subsurface water chemistry (Ackerer et al., 2018) and, in contrast, a
625 high spatial variability of the deep water chemistry in the watershed (Chabaux et al., 2017;
626 this study; figure 5). Because each borehole has a specific water chemical composition (figure
627 5), the fracture network in the bedrock is likely not connected between boreholes and each
628 fractured zone behaves as an independent system. Shallow subsurface and deep water
629 circulations also contrast by the difference of water velocities. Mean pore velocities are low
630 in the deep water system (0.5 – 3.5 m. yr^{-1}) and much higher in the shallow subsurface of the
631 watershed (1000 – 3000 m. yr^{-1}; Ackerer et al., 2020a). Such difference of water velocities

implies that the mean transit time of water is much longer in the deep CZ. Mean water transit time in the shallow subsurface is typically ranging between 1 and 4 months (Ackerer et al., 2020a), while the reactive transport modeling of the deep water chemistry indicates transit times of several hundreds of years in the deep CZ (100 – 600 yrs; this study). The spatial variability of mean transit time is therefore also higher for the deep water circulation, depending on the borehole and the fractured zone.

From the mineralogical point of view, the shallow subsurface water is in contact with a porous regolith showing a relatively homogeneous mineralogy while the deep water circulation occurs along independent fractures with a unique mineralogy. Carbonate minerals were never observed in the soil or in the regolith of the watershed (Fichter et al., 1998; Ackerer et al., 2016), and Ca^{2+} and Mg^{2+} concentrations in the shallow subsurface water are primarily controlled by the dissolution of apatite, anorthite and biotite (Goddéris et al., 2006; Ackerer et al., 2018). These primary minerals are rather homogeneously dispersed in the regolith, promoting the modest spatial variability of Ca^{2+} and Mg^{2+} concentrations in the shallow subsurface water at the watershed scale (figure 5). The presence of secondary carbonate minerals in the fracture network favors higher Ca^{2+} and Mg^{2+} concentrations in the deep water. Furthermore, the highly variable amounts of these carbonates from one fractured zone to another explain the stronger variability of Ca^{2+} and Mg^{2+} concentrations between boreholes (figure 5). The trend in H_4SiO_4 and Na^+ is more continuous between shallow subsurface and deep waters because the proportions of primary silicate minerals are less variable from the regolith to the fracture rocks. The mean dissolution rate of primary silicate minerals is on average 50-100 times lower in the fractures compared to the shallow subsurface due to the lower mean pore velocity and the longer mean transit time.

655 The difference of chemical water composition between shallow subsurface and deep waters
656 is also reinforced by a state of chemical equilibrium reached for several minerals in the deep
657 CZ. Previous reactive transport modeling studies indicated that the primary minerals as biotite
658 and K-feldspar never reach a state of chemical equilibrium in the shallow subsurface due to
659 the fast flow and the short transit time in the regolith (Ackerer et al., 2020a). This study
660 focusing on the deep water shows that a state of chemical equilibrium can be reached in the
661 deep CZ for biotite and K-feldspar (figure 7a). Chemical equilibrium of these minerals limits
662 the increase of H_4SiO_4 and K^+ in the deep water, explaining why H_4SiO_4 and K^+ concentrations
663 are only 2-3 times higher in the deep water while mean transit time is much longer in the
664 fractures. In contrast, albite never reaches a state of chemical equilibrium in the deep CZ and
665 Na^+ concentrations gradually increase with the mean transit time. Na^+ concentrations reach a
666 maximum value for the deep water with the longest transit time in F8 27 m.

667 The dynamic of clay minerals also plays a role in contrast to chemical composition between
668 shallow subsurface and deep waters. The precipitation rate of the clay solid solution is 50-100
669 times lower in the fractures than in the shallow subsurface due to the higher pH and the
670 limiting concentrations of aluminum in the deep water. The nature of clay minerals
671 precipitated along the fractures is also different from the clay minerals formed in the shallow
672 subsurface. The solid solution of clay minerals precipitated in the fractures is only composed
673 of Montmorillonites (figure 7d), while the solid solution in the shallow subsurface is made up
674 with a combination of Illites and Montmorillonites (Ackerer et al., 2020a). Montmorillonites
675 incorporate higher amount of K and Si than Illites, limiting the increase of H_4SiO_4 and K^+
676 concentrations in the deep water. In contrast to this, only few Na is incorporated in the clay
677 solid solution which promotes the gradual increase of Na^+ concentrations along fractures and
678 the higher Na^+ concentrations in the deep water with longer mean transit time (F5 45 m and

679 F8 27 m). The amounts of Mg and Ca incorporated in the clay solid solution remain limited
680 compared to the high fluxes of Mg and Ca from dissolution of dolomite, apatite and anorthite.
681 Illites, iron hydroxides, goethite and micro quartz are not precipitated in the simulations
682 capturing the chemical composition of the deep water, indicating that these minerals were
683 probably formed during different conditions in the past (higher temperature water-rock
684 interactions; hydrothermal alteration; El Gh'Mari, 1995; Fichter et al., 1998).

685 **7.3 Hydrologic and weathering fluxes in the deep CZ compared to the shallow subsurface**

686 By using the fracture cross sections and the mean pore velocities determined with the
687 reactive transport model, it is possible to calculate the annual water fluxes carried by the four
688 fractured zones F5 45 m, F6 63 m, F7 42 m and F8 27 m. These deep water fluxes represent a
689 negligible part of the annual water fluxes carried by the stream at the outlet, with 10 m^3/yr
690 carried by the four fractured zones versus 640 000 m^3/yr carried by the stream. Despite the
691 fact that we investigated the largest fractured zones in the boreholes, the deep water has a
692 limited role with respect to water fluxes at the watershed scale.

693 The finding that the deep water accounts for a negligible part of the total water fluxes is in
694 accordance with several investigations conducted so far in the Strengbach watershed. The
695 hydrologic budget of the watershed is correctly closed within uncertainties when only
696 considering mean annual precipitations (1400 mm/yr), mean evapotranspiration (600
697 mm/yr), and mean runoff at the outlet (800 mm/yr; Viville et al., 2012; Pierret et al., 2018).
698 Water discharge in the Strengbach stream is correctly modeled solely with a shallow
699 subsurface water storage in the regolith (aquifer thickness of 1-10 m; Weill et al., 2017; 2019;
700 Ackerer et al., 2020a). This is also in accordance with results inferred from hydrograph

701 separation concluding that streamflow is dominated by water mobilized from regolith layers
702 (Ladouche et al., 2001).

703 By combining the chemical composition of the deep water and the mean pore velocity along
704 the fractures, it is also possible to estimate the geochemical fluxes carried by the deep water
705 along fractures. In addition, the solute concentrations, water velocity and geochemical fluxes
706 in the shallow subsurface system are constrained from previous monitoring and reactive
707 transport modeling studies (Viville et al., 2012; Ackerer et al., 2018; 2020a). Despite the higher
708 concentrations in the deep water (figure 5), the lower mean pore velocity along the fractures
709 limits the geochemical fluxes carried by the deep water. Basic cation and dissolved silica
710 concentrations in the deep water are in general 2 to 20 times higher than the concentrations
711 in the shallow subsurface water, but the mean pore velocity is approximately 1000 to 2000
712 times faster in the shallow subsurface, implying that the contribution of the deep water to
713 the total geochemical fluxes exported from the watershed is minor (0.8-4 %, table 5). For Na^+,
714 K^+ and H_4SiO_4, the contributions of the deep water are 0.6-2.7 %, 0.3-1.4 % and 0.5-2.4 %,
715 respectively (table 5). The contribution is slightly higher for Ca^{2+} and Mg^{2+} due to the
716 dissolution of carbonate minerals along the fractures, with contributions of 3.3-19.5 % and
717 4.6-14.5 %, respectively (table 5). Overall, the deep water circulation contributes for less than
718 0.8-4 % of the total geochemical fluxes exported from the watershed (table 5). The mobility
719 of elements along a regolith profile located on the top of the watershed also indicated that
720 shallow weathering processes (0-15 m) are sufficient to explain the geochemical fluxes carried
721 by the stream (Ackerer et al., 2016).

722 The limited role of deep weathering processes is also supported by other observations. When
723 looking at the chemical composition of the Strengbach stream water in a H_4SiO_4/Cl^- vs Ca^{2+}/Cl^-

724 mixing diagram, the stream water clearly falls in the area defined by spring and piezometer
725 waters (figure 10). A mixing analysis including two end members defined by the average
726 chemical composition of stream and deep waters was performed to test which contribution
727 of deep water is potentially present in the stream. Because the deep water has a much higher
728 Ca^{2+}/Cl^{-} ratio than the stream water, the maximum contribution of deep water in the stream
729 flow is around 2 % (figure 10). A higher contribution of deep water would deviate the stream
730 chemistry toward values of Ca^{2+}/Cl^{-} ratio that were never observed in the stream. In a
731 watershed like the Strengbach watershed, the deep water circulation (20-60 m) is probably
732 not an important process in shaping the concentration-discharge relations at the stream
733 outlet. All these considerations show that the deep water circulation contributes only to a
734 negligible part of the total chemical weathering in the watershed. The exact extent of deep
735 water connectivity with the stream probably needs to be tested in future studies with more
736 accurate isotopic tools, as deep water could leave the system undetected by the stream when
737 only looking at major elements or leave the system as deep flow only relevant for inter-basin
738 circulations.

739 **7.4 The role of deep water in CZ evolution**

740 The competition and interplay between hydrogeochemical processes involved in the shallow
741 subsurface and deep CZ in shaping the CZ structure have recently received a growing interest
742 from the scientific community (e.g. Brantley et al., 2013; Buss et al., 2013; Chabaux et al.,
743 2017; Riebe et al., 2017; Holbrook et al., 2019; White et al., 2019). The extensive database
744 and the modeling work undertaken in the Strengbach watershed allow to revisit the
745 discussion on the respective role of shallow subsurface and deep water processes at the scale
746 of a headwater watershed.

747 Our results show that in the setting of a mountainous and granitic catchment, the deep water
748 is an atypical component of the hydrologic cycle with a negligible role in hydrogeochemical
749 budgets. This finding advocates for an up-bottom control of the CZ evolution because the
750 dynamic of this type of watershed is primarily driven by surface erosion, high water fluxes,
751 and fast weathering rates in the shallow subsurface (figure 11). These surface and shallow
752 subsurface processes are controlling the downward migration of weathering fronts and the
753 overall chemical weathering (Viville et al., 2012; Ackerer et al., 2016; 2020a), while the slower
754 processes occurring in the fracture network of the bedrock are unable to adjust with the
755 geochemical fluxes and the evolution rate of the near surface environment (this study, section
756 7.3). Our study therefore does not support the hypothesis that drainage of chemically
757 equilibrated water into the bedrock is an important process (Rempe and Dietrich, 2014;
758 hypothesis 2 in Riebe et al., 2017), but underlines the fact that the control through erosion,
759 shallow subsurface water circulation, and fluid transit time is primarily responsible for the CZ
760 evolution (Lebedeva and Brantley, 2013; hypothesis 4 in Riebe et al., 2017).

761 Our results can also be used to revisit the concept of rock moisture at the scale of a headwater
762 watershed. Rock moisture is defined as the exchangeable water stored in the weathered
763 bedrock (Salve et al., 2012; Rempe and Dietrich, 2018). The impact of rock moisture storage
764 on the Strengbach stream is primarily controlled by the saprolite moisture storage, the
765 saprolite being hydrologically active and sustaining the majority of the stream flow at the
766 outlet (Weill et al., 2017; 2019; Ackerer et al., 2020a). Mixing calculations performed in this
767 study also support that rock moisture storage from the deep CZ cannot explain a significant
768 fraction of the stream flow (figure 10). Therefore, our study and previous modeling studies
769 undertaken in the catchment clearly emphasize that the active rock moisture storage is
770 located in the saprolite, while the fractured bedrock contains mostly inactive rock moisture

771 storage at the watershed scale. The rock moisture storage within the saprolite should not be
772 confounded with the rock moisture storage in the fractured bedrock.

773 This conclusion contrasts with the results from several recent studies where the deep water
774 from fractured aquifer systems significantly contributes to streamflow (e.g. Frisbee et al.,
775 2017; White et al, 2019). These differences are possibility explained by the geological setting.
776 Our findings can probably be extended to small watersheds with a crystallin bedrock, but
777 different conclusions are possible for karstic or volcanic systems. In these hydrogeologic
778 systems, large and connected fractures can carry high water fluxes into the bedrock and
779 sustain stream flow (White et al., 2019). This is not the case in a headwater granitic watershed
780 like the Strengbach watershed where the stream chemistry is fully explained by the shallow
781 subsurface water (figure 10).

782 Possibly, the deep water circulation plays a role at a larger spatial scale in the Rhine graben,
783 where a regional flow of deep water from the Vosges massif may recharge deep aquifers in
784 the Rhine alluvial plain (mountain block recharge; Ajami et al., 2011; Markovich et al., 2019).
785 The role of bedrock geology (distribution and thickness of Mesozoic sedimentary cover, e.g.
786 sandstone) or the large Hercynian deformation zones in the Vosges massif might have
787 different properties with respect to water circulation and storage. Based on our results,
788 however, the ability of headwater watersheds to generate an important regional circulation
789 of deep water appears limited in crystallin landscapes, as the hydrologic budget of the
790 Strengbach watershed is correctly closed without invoking a deep water storage. The mean
791 annual precipitations of 1400 mm/yr are well partitioned between mean evapotranspiration
792 of 600 mm/yr and mean runoff at the outlet of 800 mm/yr (Viville et al., 2012; Pierret et al.,
793 2018).

794 The conclusions brought by our study are applicable from annual to millennial timescales
795 because the timeframe spanned by the mean transit time of shallow subsurface and deep
796 waters ranges from few months to 600 years. The comparison between shallow subsurface
797 and deep weathering fluxes is therefore relevant at this timescale, but it is questionable to
798 extrapolate these estimates at the million year timescale. A coupling between tectonic
799 forcing, topographic stress, and the deep water circulation initiating the bedrock weathering
800 is possible and has been highlighted by previous studies (Slim et al., 2015; St Clair et al., 2015;
801 Hypothesis 1 in Riebe et al., 2017). Our results indicate that this coupling is not dominant at
802 the millennial timescale in a granitic headwater watershed, but it may become critical at the
803 geologic timescale. If this is true, the control on the CZ evolution would be shifting from a
804 bottom-up to an up-bottom control from geologic to millennial timescale. In any case, the
805 majority of the fresh water available for water supply at a human timescale originates from
806 stream, spring, and shallow subsurface waters in this type of granitic headwater watershed.
807 The deep water circulation is too low for being critical at a timescale relevant for water supply
808 and societal needs in this type of geological context.

809 **8. Conclusion**

810 Major fractures from four boreholes and deep water collected from these fractures were
811 studied to improve our understanding of deep water circulation and of weathering processes
812 in the deep CZ of a headwater watershed. Geochemical analysis indicates that chemical
813 composition of deep water (20-60 m of depth) is clearly different from shallow subsurface
814 waters (0-15 m), with higher mean concentrations and a larger spatial variability across the
815 watershed. Our reactive transport modeling study highlights the role of dolomite dissolution
816 and of longer mean transit time in the deep CZ for explaining these differences. The modeling

results also throw light on the difference of hydrogeochemical functioning between shallow subsurface and deep systems: if the shallow system is characterized by relatively homogeneous flow, high mean pore velocities, and water-rock interactions in a porous regolith, the deep water circulation behaves much more as an independent system along fractures, with low mean pore velocities, and variable mineralogy and hydrodynamic conditions. A state of chemical equilibrium can be reached in the deep CZ for some primary minerals (biotite and K-feldspar), a feature never observed in the simulations of shallow subsurface water chemical composition in the Strengbach watershed. Even if the deep water exhibits higher concentrations, significantly lower mean pore velocities inferred in the fractured zones imply that the deep water is only responsible for a negligible part of the total hydrologic and weathering fluxes in the watershed. The limited role of the deep weathering processes (20-60 m) compared to the shallow subsurface processes (0-15 m) suggests an up to bottom control of the CZ evolution, at least at a millennial timescale and in this type of granitic headwater watershed. Our study also indicates that the majority of fresh water available for water supply at a human timescale originates from shallow subsurface waters, as the deep water circulation is too slow for being critical at a timescale relevant for water supply and societal needs in this type of geological context.

Acknowledgement

This study was financially supported by the French ANR program under grant agreement ANR-15-CE06-0014 (Project CANTARE-Alsace) and by the LabEx program G-eau-thermie profonde in Strasbourg University. Core drilling campaigns were funded by the REALISE program (CPER Alsace 2005). The authors also would like to thank Jeffrey G. Catalano, executive editor, Lixin

Jin, associate editor, and three anonymous reviewers for their very constructive and helpful comments.

References

Ackerer J., Chabaux F., Van der Woerd J., Viville D., Pelt E. and Kali E., et al. (2016) Regolith evolution on the millennial timescale from combined U–Th–Ra isotopes and in situ cosmogenic 10Be analysis in a weathering profile (Strengbach catchment, France). *Earth Planet. Sci. Lett.* **453**, 33-43.

Ackerer J., Chabaux F., Lucas Y., Clément A., Fritz B. and Beaulieu E., et al. (2018) Monitoring and reactive-transport modeling of the spatial and temporal variations of the Strengbach spring hydrochemistry. *Geochim. Cosmochim. Acta*, **225,** 17-35.

Ackerer J., Jeannot B., Delay F., Weill S., Lucas Y. and Fritz B., et al. (2020a) Crossing hydrological and geochemical modeling to understand the spatiotemporal variability of water chemistry in a headwater catchment (Strengbach, France). *Hydrol. Earth Syst. Sci.*, **24**, 3111-3133.

Ackerer J., Steefel C., Liu F., Bart R., Safeeq M. and O'Geen A., et al. (2020b) Determining How Critical Zone Structure Constrains Hydrogeochemical Behavior of Watersheds: Learning From an Elevation Gradient in California's Sierra Nevada. *Front. Water 2: 23. doi: 10.3389/frwa*.

Ajami H., Troch P. A., Maddock III T., Meixner T. and Eastoe C. (2011) Quantifying mountain block recharge by means of catchment-scale storage-discharge relationships. *Water Resources Research*, **47**.

Bales R., Molotch N. P., Painter T. H., Dettinger M. D., Rice R. and Dozier J. (2006) Mountain hydrology of the western United States. *Water Resources Research*, **42**.

Battiato I., Tartakovsky D. M., Tartakovsky A. M. and Scheibe T. D. (2011) Hybrid models of reactive transport in porous and fractured media. *Advances Water Resources*, **34**, 1140-1150.

Brantley S. L., Goldhaber M. B. and Ragnarsdottir K. V. (2007) Crossing disciplines and scales to understand the critical zone. *Elements*, **3**, 307-314.

Brantley S. L., Holleran M. E., Jin L. and Bazilevskaya E. (2013) Probing deep weathering in the Shale Hills Critical Zone Observatory, Pennsylvania (USA): the hypothesis of nested chemical reaction fronts in the subsurface. *Earth Surf. Process. Land.*, **38**, 1280-1298.

Brantley S. L., Lebedeva M. I., Balashov V. N., Singha K., Sullivan P. L. and Stinchcomb G. (2017) Toward a conceptual model relating chemical reaction fronts to water flow paths in hills. *Geomorphology*, **277**, 100-117.

Buss H. L., Brantley S. L., Scatena F. N., Bazilievskaya E. A., Blum A. and Schulz M. et al. (2013) Probing the deep critical zone beneath the Luquillo Experimental Forest, Puerto Rico. *Earth Surf. Process. Land.,* **38**, 1170-1186.

Chabaux F., Viville D., Lucas Y., Ackerer J., Ranchoux C. and Bosia C. et al. (2017) Geochemical tracing and modeling of surface and deep water–rock interactions in elementary granitic watersheds (Strengbach and Ringelbach CZOs, France). *Acta Geochim.*, **36**, 363-366.

Chabaux F., Stille P., Prunier J., Gangloff S., Lemarchand D. and Morvan G. et al. (2019) Plant-soil-water interactions: Implications from U-Th-Ra isotope analysis in soils, soil solutions and vegetation (Strengbach CZO, France). *Geochim. Cosmochim. Acta*, **259**, 188-210.

Clair J. S., Moon S., Holbrook W. S., Perron J. T., Riebe C. S. and Martel S. J. et al. (2015) Geophysical imaging reveals topographic stress control of bedrock weathering. *Science*, **350**, 534-538.

Chorover J., Troch P. A., Rasmussen C., Brooks P. D., Pelletier J. D. and Breshears D. D. et al. (2011) How water, carbon, and energy drive critical zone evolution: The Jemez–Santa Catalina Critical Zone Observatory. *Vadose Zone Journal*, **10**, 884-899.

Daval D., Calvaruso C., Guyot F. and Turpault M. P. (2018) Time-dependent feldspar dissolution rates resulting from surface passivation: Experimental evidence and geochemical implications. *Earth Planet. Sci. Lett.*, **498**, 226-236.

Deng H., Molins S., Steefel C., DePaolo D., Voltolini M. and Yang L. et al. (2016) A 2.5 D reactive transport model for fracture alteration simulation. *Environ. Sci. Tech.*, **50**, 7564-7571.

889 Deng H. and Spycher N. (2019) Modeling reactive transport processes in fractures. *Rev. Min.*
890 *Geochem.*, **85**, 49-74.
891 Dezayes C. and Lerouge C. (2019) Reconstructing paleofluid circulation at the Hercynian
892 basement/Mesozoic sedimentary cover interface in the Upper Rhine Graben. *Geofluids*.
893 Dralle D. N., Hahm W. J., Rempe D. M., Karst N. J., Thompson S. E. and Dietrich W. E. (2018)
894 Quantification of the seasonal hillslope water storage that does not drive streamflow. *Hydrol.*
895 *Process.*, **32**, 1978-1992.
896 El Gh'Mari A. (1995) Étude pétrographique, minéralogique et géochimique de la dynamique
897 d'altération d'un granité soumis aux dépôts atmosphériques acides (bassin versant du
898 Strengbach, Vosges, France): mécanisme, bilan et modélisation. PhD Thesis. Université Louis
899 Pasteur. France. pp 200.
900 Fan Y., Miguez-Macho G., Jobbágy E. G., Jackson R. B. and Otero-Casal C. (2017) Hydrologic regulation
901 of plant rooting depth. *Proceed. Nat. Aca. Sciences*, **114**, 10572-10577.
902 Fichter J., Turpault M. P., Dambrine E. and Ranger J. (1998) Mineral evolution of acid forest soils in the
903 Strengbach catchment (Vosges mountains, NE France). *Geoderma*, **82**, 315-340.
904 Frisbee M. D., Tolley D. G. and Wilson J. L. (2017) Field estimates of groundwater circulation depths in
905 two mountainous watersheds in the western US and the effect of deep circulation on solute
906 concentrations in streamflow. *Water Resources Research, **53**, 2693-2715*.
907 Gangloff S., Stille P., Pierret M. C., Weber T. and Chabaux F. (2014) Characterization and evolution of
908 dissolved organic matter in acidic forest soil and its impact on the mobility of major and trace
909 elements (case of the Strengbach watershed). *Geochim. Cosmochim. Acta*, **130**, 21-41.
910 Gérard F., Clément A. and Fritz, B. (1998) Numerical validation of a Eulerian hydrochemical code using
911 a 1D multisolute mass transport system involving heterogeneous kinetically controlled
912 reactions. *J. Cont. Hydrol.*, **30**, 201-216.
913 Gleeson T., Befus K. M., Jasechko S., Luijendijk E. and Cardenas M. B. (2016) The global volume and
914 distribution of modern groundwater. *Nat. Geosci.*, **9**, 161-167.

915 Goddéris Y., François L. M., Probst A., Schott J., Moncoulon D. and Labat D. et al. (2006) Modelling
916 weathering processes at the catchment scale: The WITCH numerical model. *Geochim.*
917 *Cosmochim. Acta*, **70**, 1128-1147.
918 Hahm W. J., Rempe D. M., Dralle D. N., Dawson T. E., Lovill S. M. and Bryk A. B. et al. (2019)
919 Lithologically controlled subsurface critical zone thickness and water storage capacity
920 determine regional plant community composition. *Water Resources Research*, **55**, 3028-3055.
921 Heidari P., Li L., Jin L., Williams J. Z. and Brantley S. L. (2017) A reactive transport model for Marcellus
922 shale weathering. *Geochim. Cosmochim. Acta*, **217**, 421-440.
923 Holbrook W. S., Riebe C. S., Elwaseif M., L. Hayes J., Basler-Reeder K., L. and Harry D. et al. (2014)
924 Geophysical constraints on deep weathering and water storage potential in the Southern
925 Sierra Critical Zone Observatory. *Earth Surf. Process. Land.*, **39**, 366-380.
926 Holbrook W. S., Marcon V., Bacon A. R., Brantley S. L., Carr B. J. and Flinchum B. A. et al. (2019) Links
927 between physical and chemical weathering inferred from a 65-m-deep borehole through
928 Earth's critical zone. *Sci. report*., **9**, 1-11.
929 Kim H., Dietrich W. E., Thurnhoffer B. M., Bishop J. K. and Fung I. Y. (2017) Controls on solute
930 concentration-discharge relationships revealed by simultaneous hydrochemistry observations
931 of hillslope runoff and stream flow: The importance of critical zone structure. *Water Resources*
932 *Research*, **53**, 1424-1443.
933 Klos P. Z., Goulden M. L., Riebe C. S., Tague C. L., O'Geen A. T. and Flinchum B. A. et al. (2018)
934 Subsurface plant-accessible water in mountain ecosystems with a Mediterranean climate. *Wil.*
935 *Inter. Rev.: Water*, **5**.
936 Ladouche B., Probst A., Viville D., Idir S., Baqué D. and Loubet M. et al. (2001) Hydrograph separation
937 using isotopic, chemical and hydrological approaches (Strengbach catchment, France). *J.*
938 *hydrol.*, **242**, 255-274.
939 Li L., Maher K., Navarre-Sitchler A., Druhan J., Meile C. and Lawrence C. et al. (2017). Expanding the
940 role of reactive transport models in critical zone processes. *Earth-science rev.*, **165**, 280-301.

941 Lichtner P. C. (1988) The quasi-stationary state approximation to coupled mass transport and fluid-
942 rock interaction in a porous medium. *Geochim. Cosmochim. Acta*, **52**, 143-165.
943 Liu F., Conklin M. H. and Shaw G. D. (2017) Insights into hydrologic and hydrochemical processes based
944 on concentration-discharge and end-member mixing analyses in the mid-Merced River Basin,
945 Sierra Nevada, California. *Water Resources Research*, **53**, 832-850.
946 Lucas Y., Chabaux F., Schaffhauser T., Fritz B., Ambroise B. and Ackerer J. et al. (2017)
947 Hydrogeochemical modeling (KIRMAT) of spring and deep borehole water compositions in the
948 small granitic Ringelbach catchment (Vosges Mountains, France). *Appl. Geochem.*, **87**, 1-21.
949 Lucas Y., Ngo V. V., Clément A., Fritz B. and Schäfer G. (2020) Modelling acid stimulation in the
950 enhanced geothermal system of Soultz-sous-Forêts (Alsace, France). *Geothermics*, **85**,
951 101772.
952 MacQuarrie K. T. and Mayer K. U. (2005) Reactive transport modeling in fractured rock: A state-of-
953 the-science review. *Earth-Science Rev.*, **72**, 189-227.
954 Maher K. (2011) The role of fluid residence time and topographic scales in determining chemical fluxes
955 from landscapes. *Earth Planet. Sci. Lett.*, **312**, 48-58.
956 Markovich K. H., Manning A. H., Condon L. E. and McIntosh J. C. (2019) Mountain-block recharge: A
957 review of current understanding. *Water Resources Research*, **55**, 8278-8304.
958 Meakin P. and Tartakovsky A. M. (2009) Modeling and simulation of pore-scale multiphase fluid flow
959 and reactive transport in fractured and porous media. *Rev. Geophy*., **47**.
960 M'Nassri S., Lucas Y., Schäfer G., Dridi L. and Majdoub R. (2019) Coupled hydrogeochemical modelling
961 using KIRMAT to assess water-rock interaction in a saline aquifer in central-eastern Tunisia.
962 *Appl. Geochem.*, **102**, 229-242.
963 Moore J., Lichtner P. C., White A. F. and Brantley S. L. (2012) Using a reactive transport model to
964 elucidate differences between laboratory and field dissolution rates in regolith. *Geochim.*
965 *Cosmochim. Acta*, **93**, 235-261.
966

967 Ngo V. V., Delalande M., Clément A., Michau N. and Fritz B. (2014) Coupled transport-reaction
968 modeling of the long-term interaction between iron, bentonite and Callovo-Oxfordian
969 claystone in radioactive waste confinement systems. *Appl. clay sci.*, **101**, 430-443.
970 O'Geen A., Safeeq M., Wagenbrenner J., Stacy E., Hartsough P. and Devine S. et al. (2018) Southern
971 Sierra Critical Zone Observatory and Kings River Experimental Watersheds: A synthesis of
972 measurements, new insights, and future directions. *Vad. Zone J.*, **17**, 1-18.
973 Pierret M. C., Cotel S., Ackerer P., Beaulieu E., Benarioumlil S. and Boucher M. et al. (2018) The
974 Strengbach catchment: A multidisciplinary environmental sentry for 30 years. *Vad. Zone J.*, **17**,
975 1-17.
976 Prunier J., Chabaux F., Stille P., Gangloff S., Pierret M. C. and Viville D. et al. (2015) Geochemical and
977 isotopic (Sr, U) monitoring of soil solutions from the Strengbach catchment (Vosges
978 mountains, France): Evidence for recent weathering evolution. *Chem. Geol.*, **417**, 289-305.
979 Ranchoux C. (2020) Caractérisation géochimique et datation des circulations d'eaux profondes dans
980 la zone critique : cas du bassin versant du Strengbach. PhD Thesis. University of Strasbourg.
981 France. pp 288.
982 Ranchoux C., Chabaux F., Viville D., Labasque T., Lucas Y., Van der Woerd J., Ackerer J., Aquilina L.
983 (2021) Characterization of groundwater circulations in a headwater catchment from an
984 analysis of chemical concentrations, Sr-Nd-U isotope ratios, and CFC, SF6 gas tracers
985 (Strengbach CZO, France). *Appl. Geochem.,* **131**, 0883-2927.
986 Riebe C. S., Hahm W. J. and Brantley S. L. (2017) Controls on deep critical zone architecture: A historical
987 review and four testable hypotheses. *Earth Surf. Process. Land*., **42**, 128-156.
988 Rempe D. M. and Dietrich W. E. (2018) Direct observations of rock moisture, a hidden component of
989 the hydrologic cycle. *Proceed. Nat. Aca. Sci.*, **115**, 2664-2669.
990 Salehikhoo F. and Li L. (2015) The role of magnesite spatial distribution patterns in determining
991 dissolution rates: When do they matter? *Geochim. Cosmochim. Acta*, **155**, 107-121.

992 Salve R., Rempe D. M. and Dietrich W. E. (2012) Rain, rock moisture dynamics, and the rapid response
993 of perched groundwater in weathered, fractured argillite underlying a steep hillslope. *Water*
994 *Resources Research*, **48**.
995 Schmitt A.D., Gangloff S., Labolle F., Chabaux F. and Stille P. (2017) Ca biogeochemical cycle at the
996 beech tree - soil solution interface from the Strengbach CZO (NE France): insights from stable
997 Ca and radiogenic Sr isotopes. *Geochim. Cosmochim. Acta, **213**, 91-109.*
998 Schulmann K., Schaltegger U., Jezek J., Thompson A. B. and Edel J. B. (2002) Rapid burial and
999 exhumation during orogeny: Thickening and synconvergent exhumation of thermally
1000 weakened and thinned crust (Variscan orogen in Western Europe). *American J. Sci*, ***302***, 856-
1001 879.
1002 Slim M., Perron J. T., Martel S. J. and Singha, K. (2015) Topographic stress and rock fracture: A two-
1003 dimensional numerical model for arbitrary topography and preliminary comparison with
1004 borehole observations. *Earth Surf. Process. Land.*, ***40***, 512-529.
1005 Steefel C. I., Appelo C. A. J., Arora B., Jacques D., Kalbacher T. and Kolditz O. et al. (2015) Reactive
1006 transport codes for subsurface environmental simulation. *Comput. Geosciences*, ***19***, 445-478.
1007 Steefel C. I. and Lichtner P. C. (1998) Multicomponent reactive transport in discrete fractures: I.
1008 Controls on reaction front geometry. *J. of Hydrol.*, ***209***, 186-199.
1009 Tardy Y. and Fritz B. (1981) An ideal solid solution model for calculating solubility of clay minerals. *Clay*
1010 *minerals*, ***16***, 361-373.
1011 Viville D., Chabaux F., Stille P., Pierret M. C. and Gangloff S. (2012) Erosion and weathering fluxes in
1012 granitic basins: The example of the Strengbach catchment (Vosges massif, eastern France).
1013 *Catena*, **92**, 122-129.
1014 Weill S., Delay F., Pan Y. and Ackerer P. (2017) A low-dimensional subsurface model for saturated and
1015 unsaturated flow processes: ability to address heterogeneity. *Comput. Geosciences*, **21**, 301-
1016 314.

1017 Weill S., Lesparre N., Jeannot B. and Delay F. (2019) Variability of Water Transit Time Distributions at
1018 the Strengbach Catchment (Vosges Mountains, France) Inferred Through Integrated
1019 Hydrological Modeling and Particle Tracking Algorithms. *Water*, **11**, 2637.
1020 West A. J. (2012) Thickness of the chemical weathering zone and implications for erosional and
1021 climatic drivers of weathering and for carbon-cycle feedbacks. *Geology*, ***40***, 811-814.
1022 White A., Moravec B., McIntosh J., Olshansky Y., Paras B. and Sanchez R. A. et al. (2019) Distinct stores
1023 and the routing of water in the deep critical zone of a snow-dominated volcanic catchment.
1024 *Hydrol. Earth Syst. Sci*., **23**, 4661-4683.
1025 Yasuhara H. and Elsworth D. (2006) A numerical model simulating reactive transport and evolution of
1026 fracture permeability. *International J. num. method. geomechanics*, **30**, 1039-1062.
1027 Zhi W., Li L., Dong W., Brown W., Kaye J. and Steefel C. et al. (2019) Distinct source water chemistry
1028 shapes contrasting concentration-discharge patterns. *Water Resources Research*, ***55***, 4233-
1029 4251.
1030

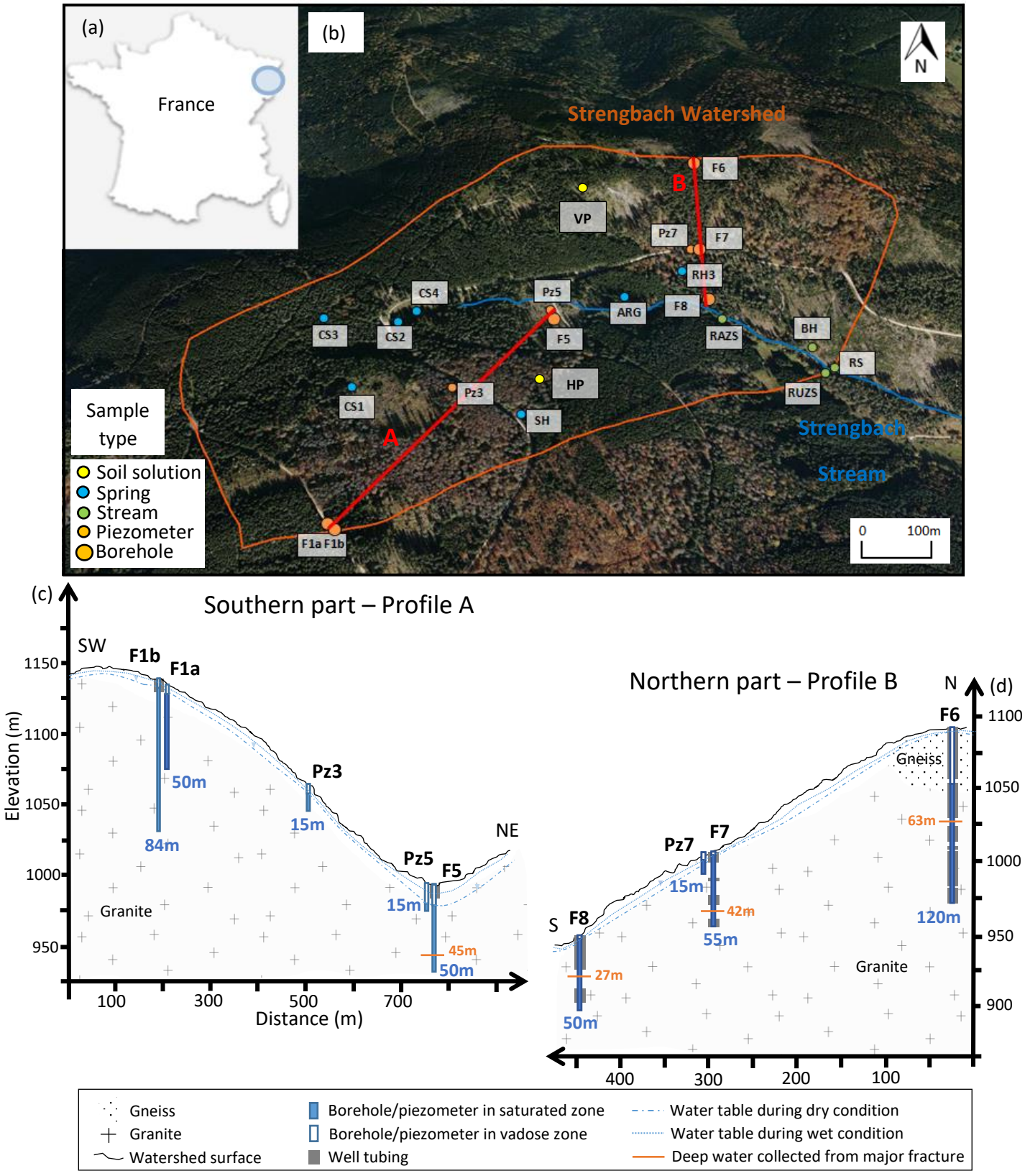

Figure 1: watershed and sampling location (a) Strengbach watershed location in northeastern France. (b) Sampling location of spring, stream, piezometer, and borehole waters within the watershed. (c) Profile A on the southern part of the watershed including F1b and F5 boreholes, and Pz3 and Pz5 piezometers. (d) Profile B on the northern part of the watershed including F6, F7 and F8 boreholes, and Pz7 piezometer.

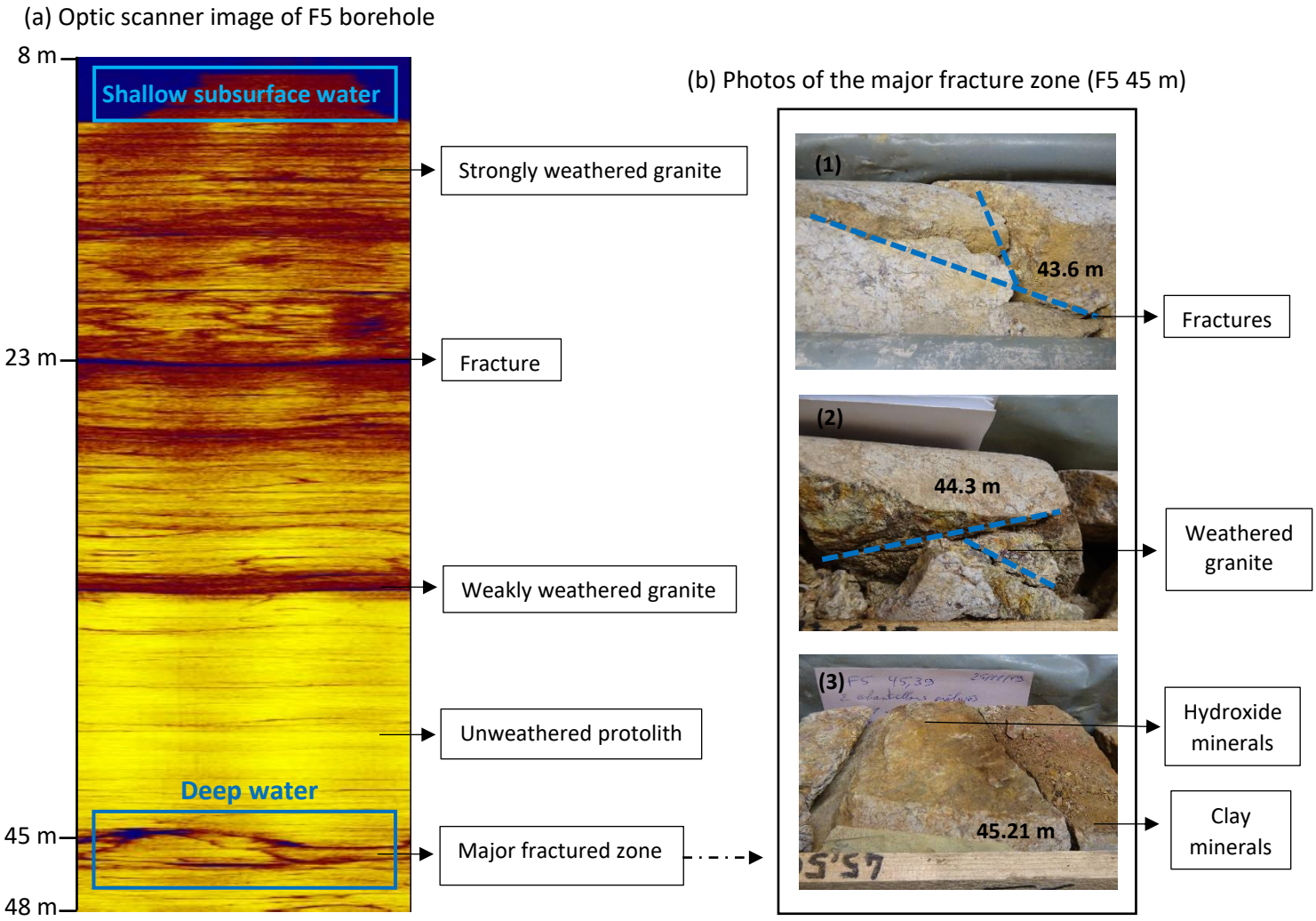

Figure 2: overview of the F5 borehole (a) Image of F5 borehole obtained from geophysical mapping of the borehole surface (optic scanner). (b) Photos of the major fracture zone at around 45 m of depth in F5. Photos were taken from drill cores and show fractures (photo 1, at 43.6 m of depth), weathered granite and secondary minerals on fracture planes (photos 2 and 3, 44.3 m and 45.21 m of depth).

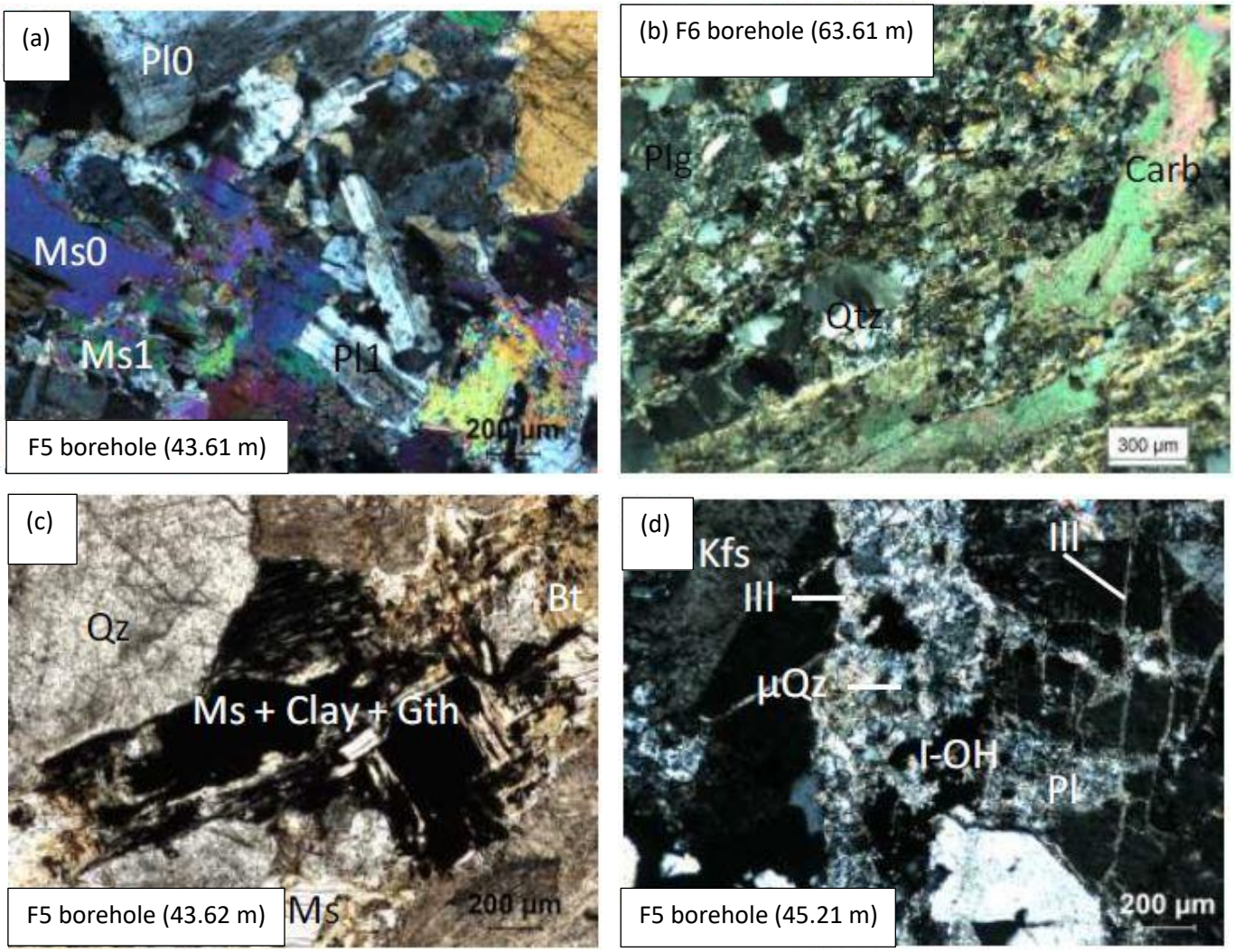

Figure 3: thin sections of rock samples collected on fracture planes intercepting deep boreholes. (a) thin section from F5 borehole showing typical mineral assemblage of the granite with plagioclase, muscovite, and quartz. (b) thin section from F6 borehole showing secondary carbonate minerals (dolomite) surrounded by quartz and plagioclase. (c) thin section from F5 showing quartz, muscovite, biotite, with typical weathering of biotite into secondary clay minerals (presence of montmorillonites, smectites, illites) and iron hydroxides. (d) thin section from F5 showing micro-quartz, plagioclase, K-feldspar, and secondary minerals (iron hydroxides and clay minerals). Abbreviations used in the figure are quartz (Qz/Qtz), micro-quartz (µQz), plagioclase (Plg/Pl), carbonates (carb), muscovite (Ms), biotite (Bt), Goethite (Gth), K-feldspar (Kfs), iron hydroxides (I-OH), clay minerals (Clay) and illites (Ill).

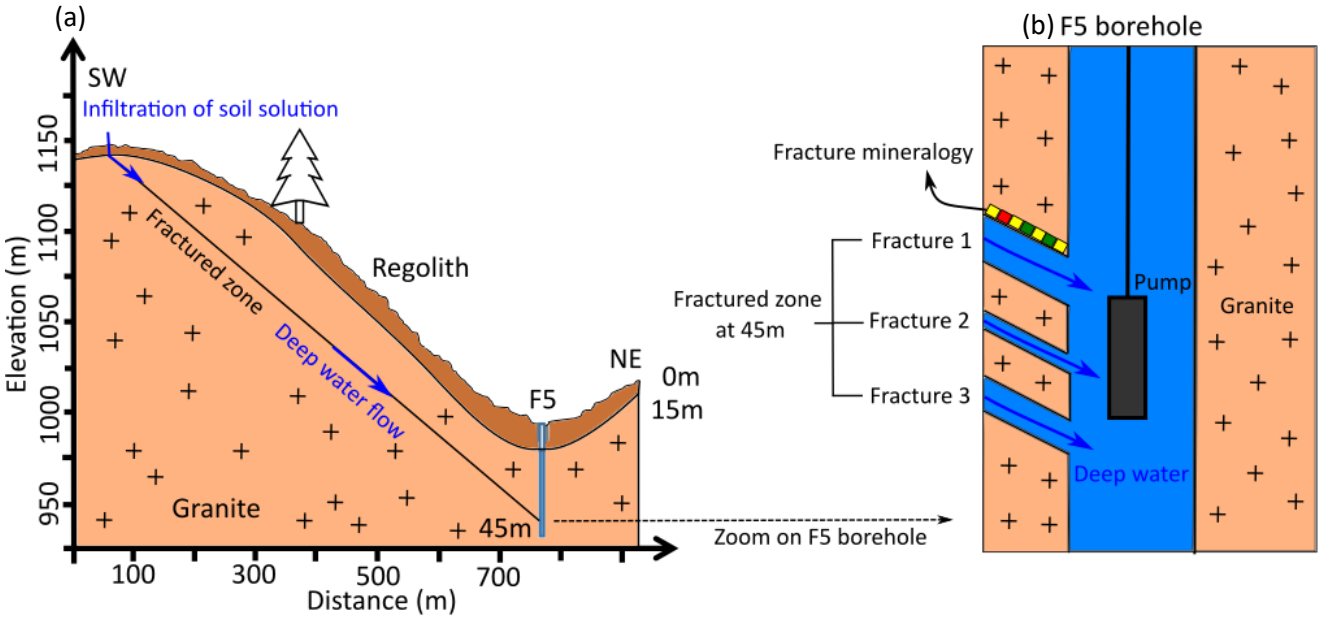

Figure 4: modeling scheme used for the reactive-transport modeling of deep water. (a) Modeling strategy at the hillslope scale shown for the F5 borehole on the southern part of the watershed. Water infiltrates on watershed crest and flows along a fractured zone intercepting the borehole (b) Zoom on the major fractured zone at F5 45 m and illustration of fractures, fracture mineralogy, and pump sampling. Minerals are illustrated by color boxes on a fracture plane. Water-rock interactions described by the reactive transport modeling as primary mineral dissolution and clay mineral precipitation occur along fracture planes.

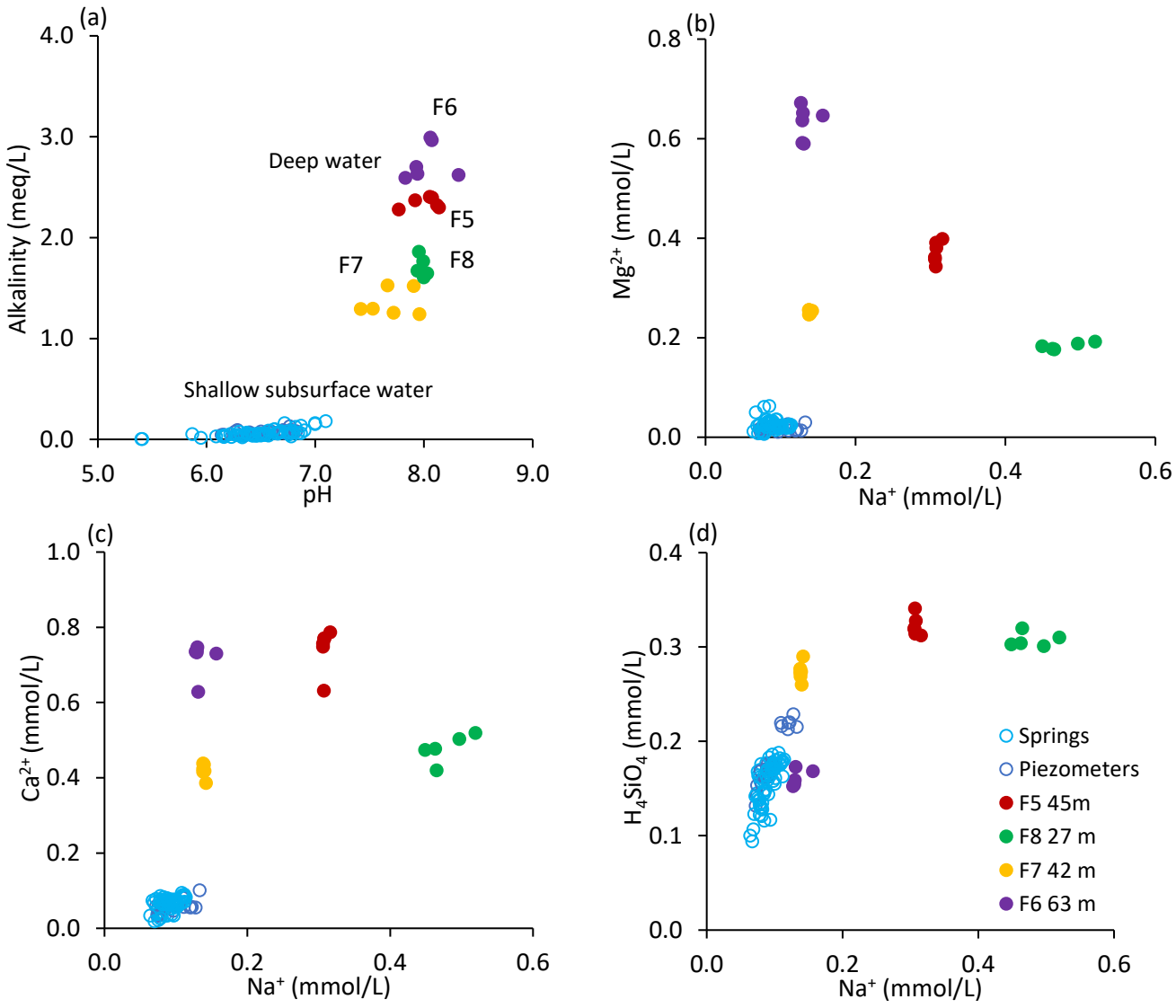

Figure 5: geochemical composition of deep and shallow subsurface waters in the Strengbach watershed (a) pH-alkalinity diagram for the Strengbach waters, including spring (3-5 m of depth), piezometer (PZ3 11 m, PZ5 15 m, PZ7 12 m) and borehole waters (F5 45 m, F6 63 m, F7 42 m, F8 27 m). (b) Mg^{2+} - Na^{+} diagram. (c) Ca^{2+} - Na^{+} diagram. (d) H_4SiO_4 - Na^{+} diagram.

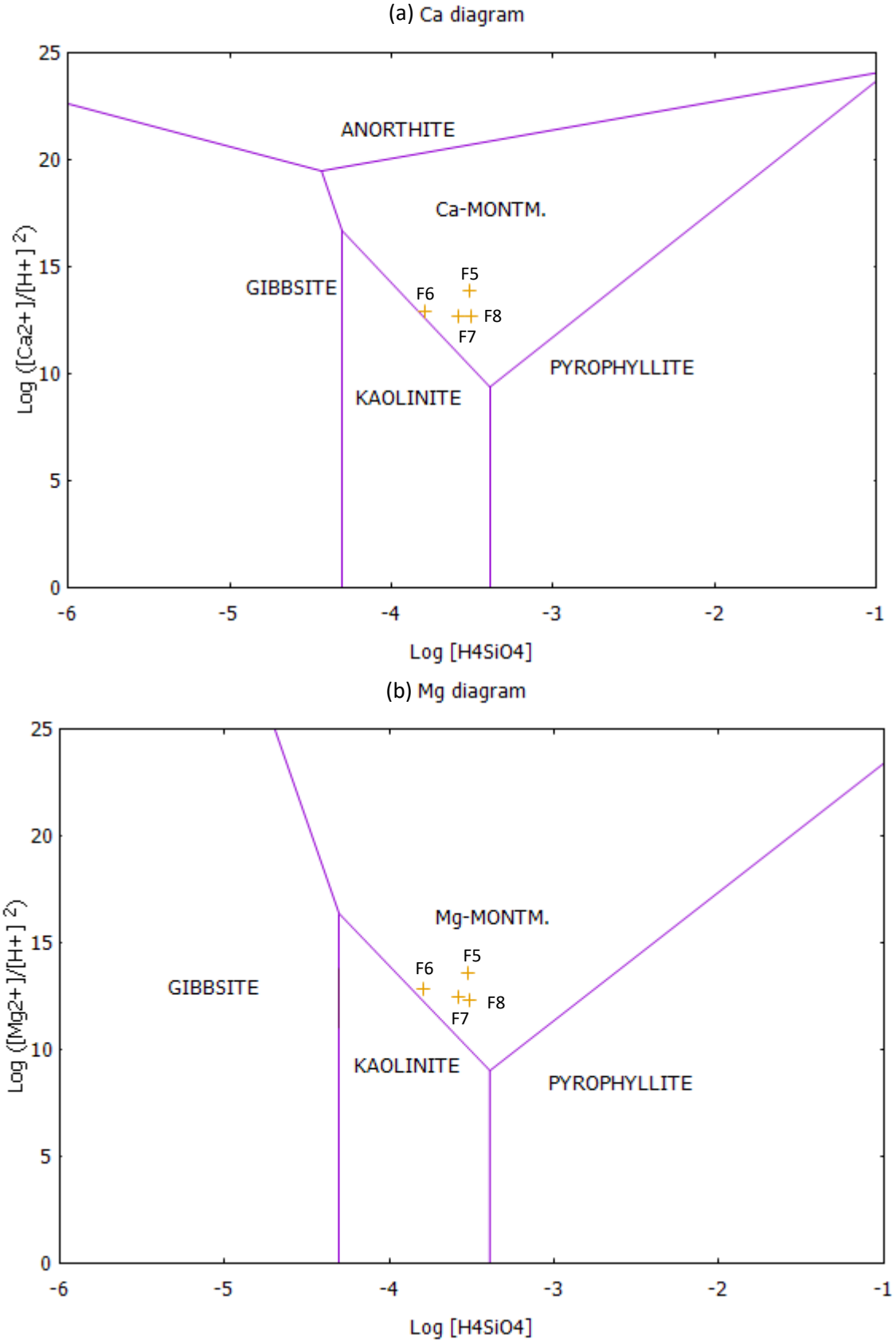

Figure 6: stability diagrams under thermodynamic conditions encountered in deep water samples collected from major borehole fractured zones. (a) diagram for Ca showing stability of Ca-montmorillonite. (b) diagram for Mg showing stability of Mg-montmorillonite. Crosses represent data points calculated from mean concentrations in borehole waters collected from F5 45 m, F6 63 m, F7 42 m and F8 27 m.

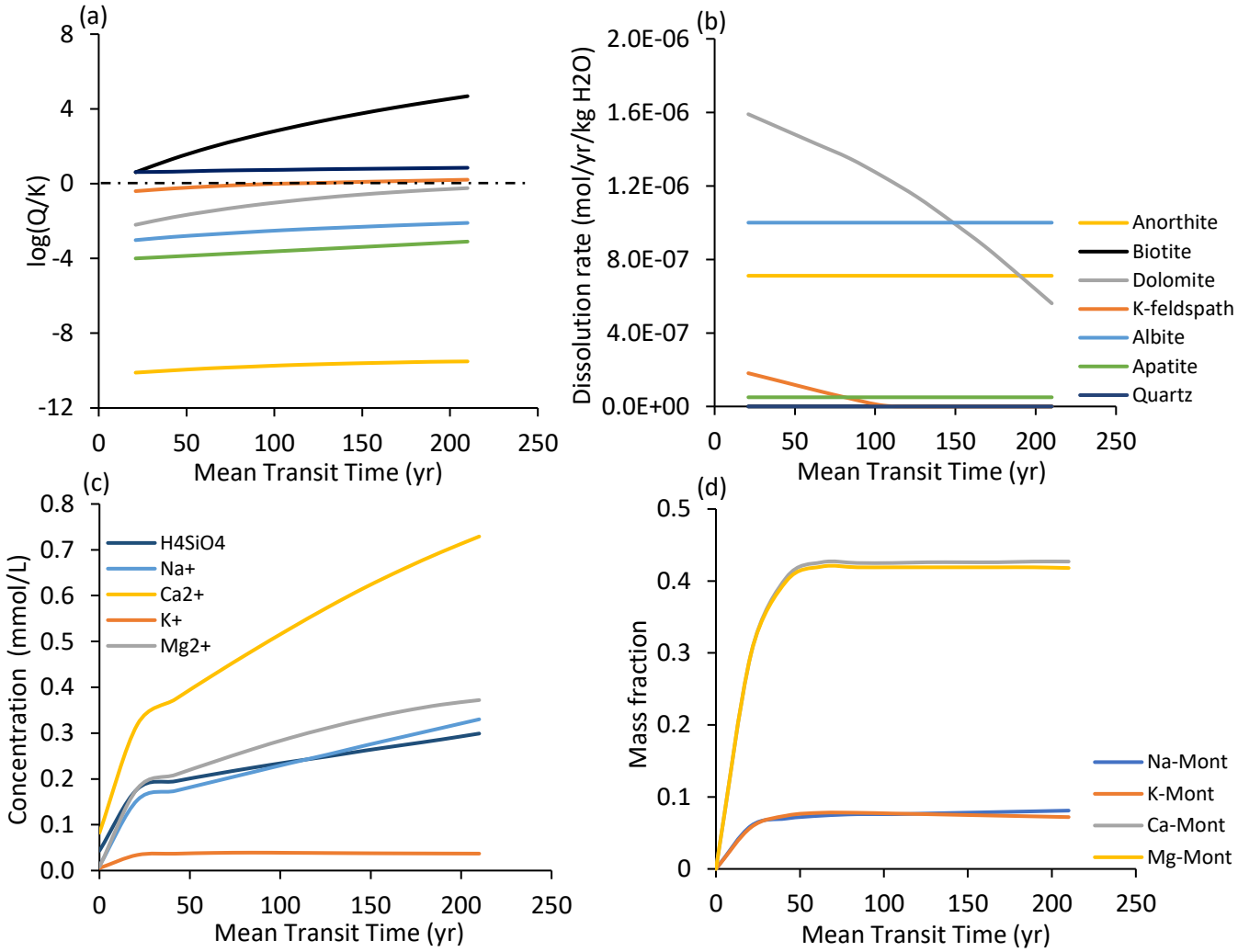

Figure 7: primary mineral saturation states, dissolution rates, solute concentrations, and clay minerals along the fracture network at F5 45m as function of mean transit time. (a) log(Q/K) of primary minerals versus mean transit time of the deep water. (b) dissolution rates of primary minerals. (c) solute concentrations of silica and basic cations. (d) mass fraction of clay end members in the clay solid solution. The end of simulation corresponds to the optimized mean transit time of 210 yrs obtained by calibration.

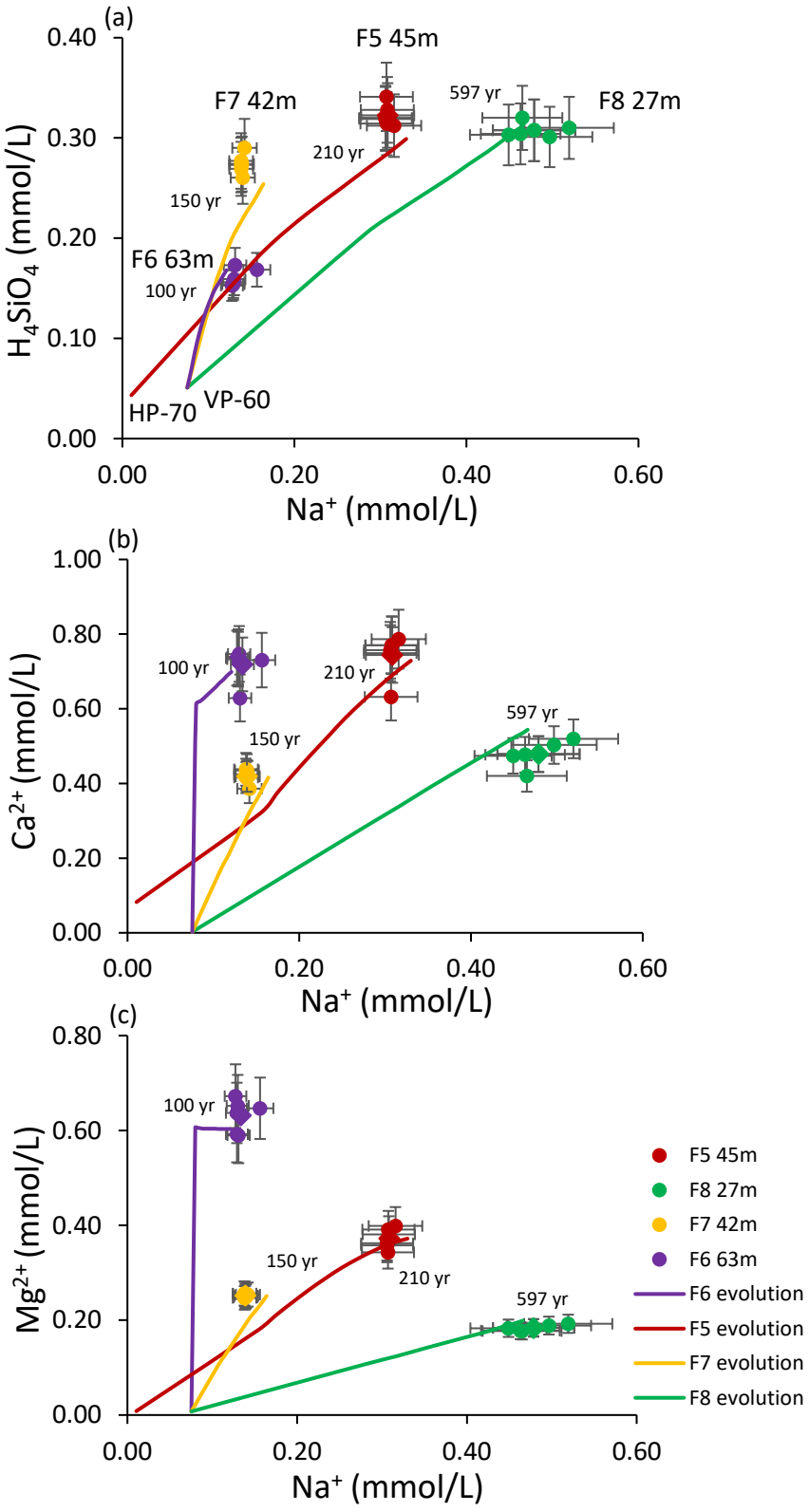

Figure 8: elementary diagrams showing the chemical composition of the deep water. Individual samples (points), mean values (diamonds), and evolution of the simulated chemical composition of the deep water along fractured zones (lines) are represented. Simulations shown on this figure targeted mean values. Initial values are soil solution values (HP-70, VP-60). (a) subplot for H_4SiO_4 and Na^+. (b) subplot for Ca^{2+} and Na^+. (c) subplot for Mg^{2+} and Na^+.

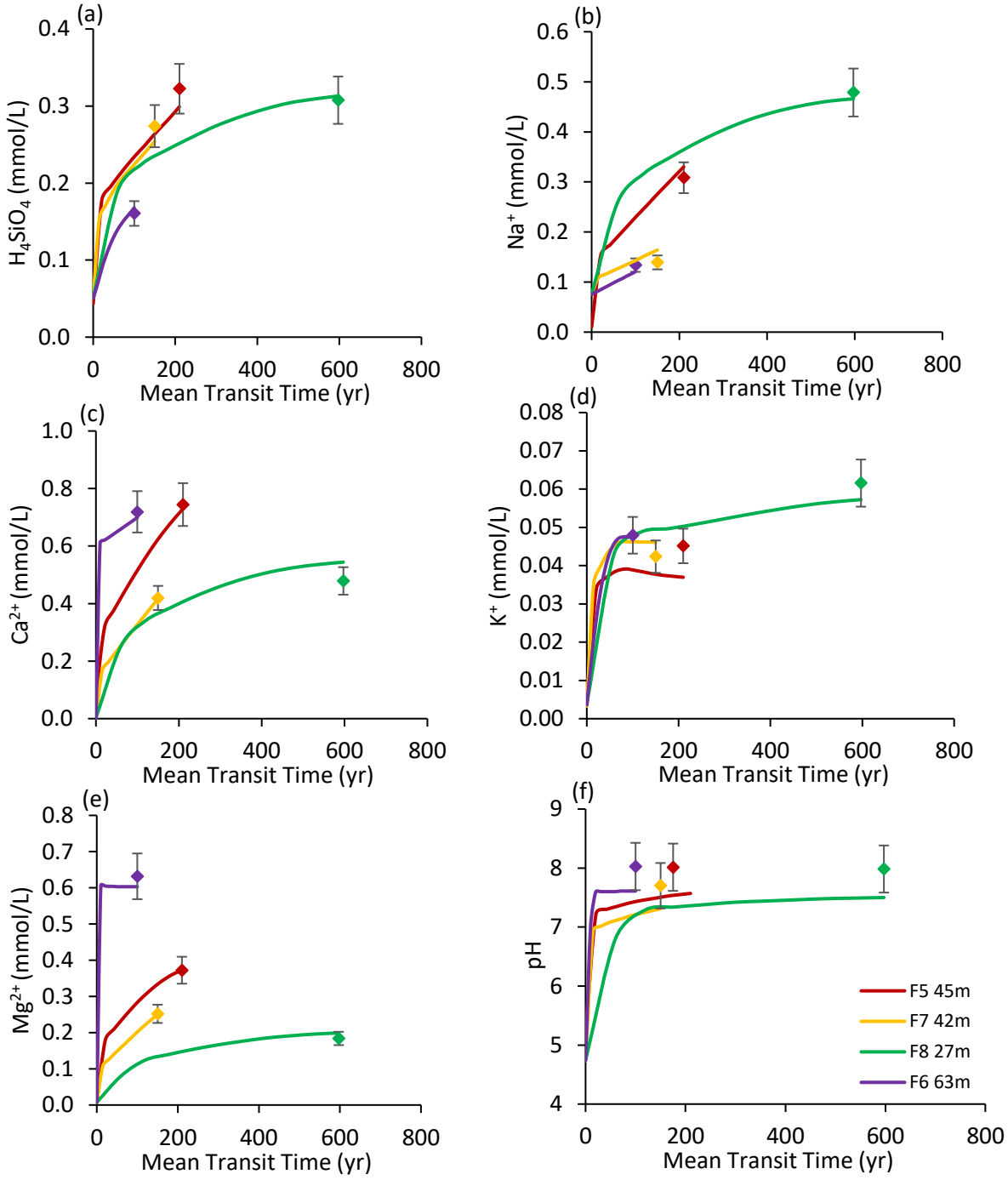

Figure 9: simulation of the deep water chemical composition and of the mean transit time along main fractured zones of F5, F6, F7 and F8 boreholes. Diamonds represent average values of measured parameters from deep water samples and lines represent simulated values. (a) subplot for H_4SiO_4. (b) subplot for Na^+. (c) subplot for Ca^{2+}. (d) subplot for K+. (e) subplot for Mg^{2+}. (f) subplot for pH.

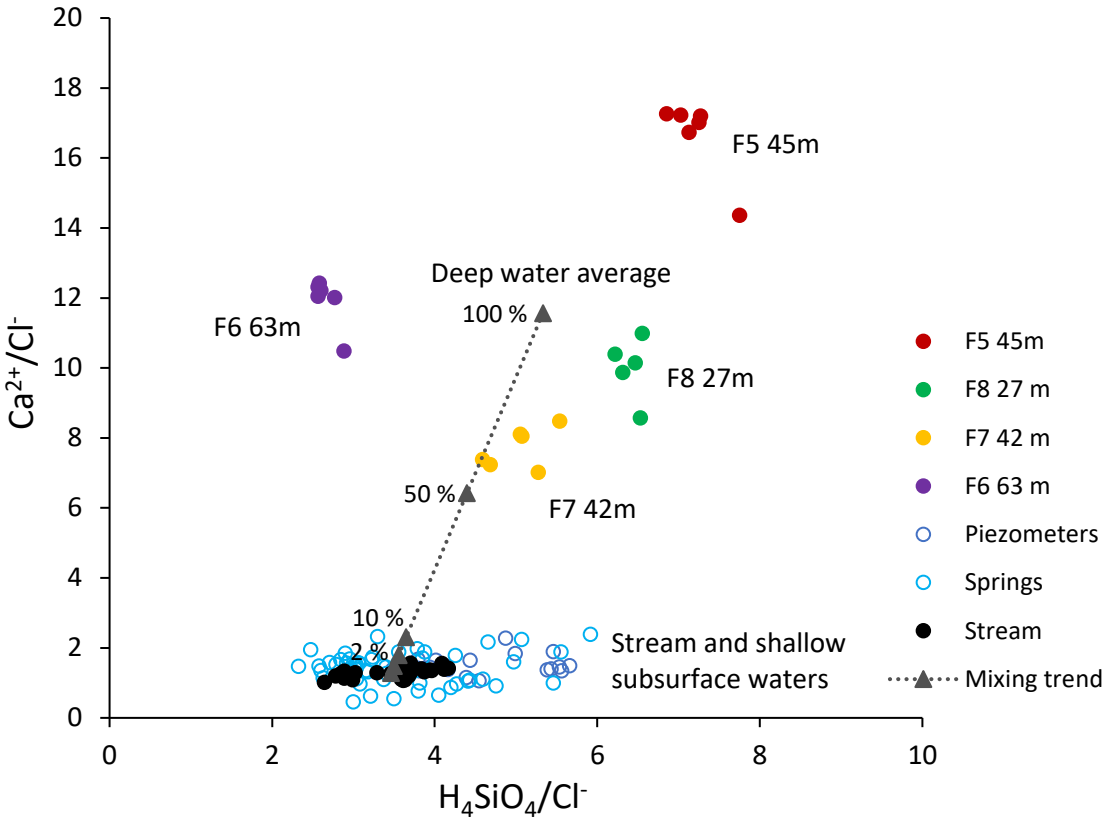

Figure 10: mixing H_4SiO_4/Cl^- vs Ca^{2+}/Cl^- diagram showing the chemical composition of the deep water (F5 45 m, F8 27 m, F7 42 m and F6 63 m), the shallow subsurface water (Strengbach springs and piezometers) and the Strengbach stream water. Mixing trend between deep water average and stream water average is shown in dotted line with deep water contribution expressed in %.

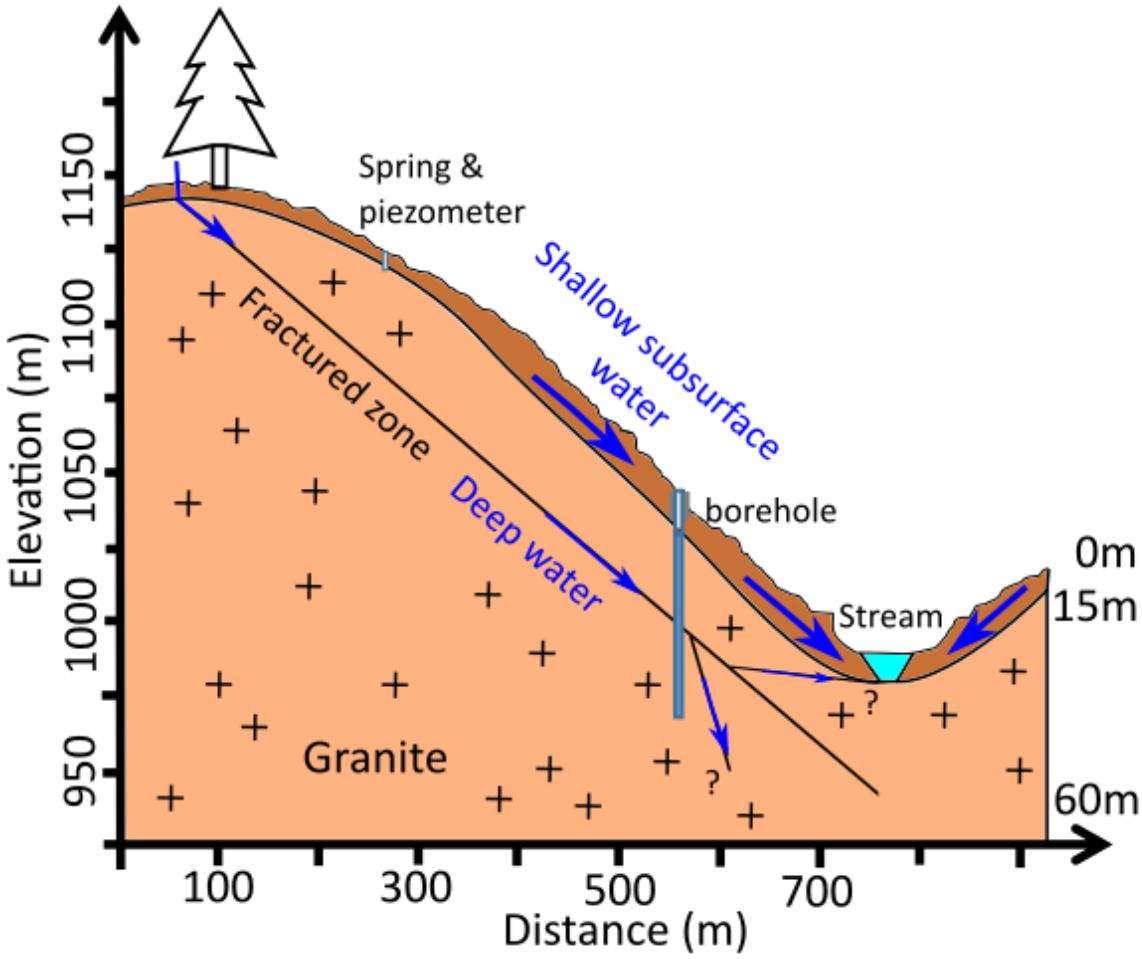

Figure 11: summary figure of the hydrogeochemical functioning of the Strengbach watershed. The shallow subsurface water carries most of the hydrological and geochemical fluxes at the watershed scale and explains most of the stream flow at the outlet. The deep water flows along independent fractures and represents only a minor part of total hydrological and geochemical fluxes. This hydrogeochemical functioning implies a up-bottom control on CZ evolution where the watershed dynamic is primarily driven by surface erosion, high water fluxes, and fast weathering rates in the shallow subsurface.

Structural data of the major fractures from boreholes F5, F6, F7 and F8 where deep water samples were taken. Geochemical analysis and reactive transport modeling of the water chemical composition were performed on water samples from these fractured zones.

Southern slope borehole		**Depth (m)**	**Azimuth (°)**	**Aperture (mm)**	**Dip (°)**	**specific surface of water-rock contact ($m^2.kg\ H_2O^{-1}$)**
F5	**fracture 1**	43.61	89	75	53	0.055
	fracture 2	44.30	96	19	40	0.016
	fracture 3	45.21	91	11	22	0.024
Northern slope boreholes		**Depth (m)**	**Azimuth (°)**	**Aperture (mm)**	**Dip (°)**	**specific surface of water-rock contact ($m^2.kg\ H_2O^{-1}$)**
F6	**fracture 1**	62.70	105	5	66	0.028
	fracture 2	63.47	175	7	9	0.034
	fracture 3	63.61	173	59	44	0.059
F7	**fracture 1**	39.96	166	23	43	0.037
	fracture 2	41.42	159	20	52	0.042
	fracture 3	42.13	143	22	56	0.050
F8	**fracture 1**	27.53	143	16	53	0.170

Table 1

Mass fractions and reactive surfaces of minerals in the major fractured zones from boreholes. Mass fractions are averaged values from the analysis of fracture planes. Reactive surfaces are given for the major fractured zones intercepting the boreholes by taking the sum of the reactive surfaces from individual fracture planes and are expressed in m^2 kg H_2O^{-1}.

Southern slope borehole		**Quartz**	**Albite**	**Anorthite**	**K-feldspar**	**Muscovite**	**Biotite**	**Apatite**	**Dolomite**
F5 45 m	**mass fraction**	0.37	0.32	0.03	0.19	0.03	0.05	0.005	0.005
	reactive surface	0.035	0.030	0.002	0.018	0.002	0.004	0.0005	0.0005
Northern slope boreholes		**Quartz**	**Albite**	**Anorthite**	**K-feldspar**	**Muscovite**	**Biotite**	**Apatite**	**Dolomite**
F6 63 m	**mass fraction**	0.38	0.27	0.02	0.24	0.02	0.06	0.005	0.010
	reactive surface	0.045	0.032	0.002	0.028	0.002	0.007	0.0006	0.001
F7 42 m	**mass fraction**	0.38	0.28	0.02	0.24	0.03	0.04	0.005	0.005
	reactive surface	0.049	0.036	0.002	0.031	0.003	0.005	0.0006	0.0006
F8 27 m	**mass fraction**	0.36	0.34	0.03	0.20	0.02	0.04	0.0050	0.0010
	reactive surface	0.061	0.057	0.005	0.034	0.004	0.007	0.0008	0.0002

Table 2

Geochemical composition of deep water collected from the major fractured zones in boreholes. Piezometric levels are expressed in m below surface, concentrations are in mmol/L and alkalinity in meq/L.

Southern slope borehole	Sampling date	Piezometric level	Alkalinity	pH	Na^+	K^+	Mg^{2+}	Ca^{2+}	H_4SiO_4
F5 45 m	27/10/2016	11.59	2.396	8.08	0.316	0.044	0.399	0.787	0.312
	23/11/2016	10.30	2.403	8.06	0.308	0.045	0.391	0.771	0.314
	10/10/2017	11.22	2.321	8.12	0.306	0.068	0.362	0.757	0.320
	10/01/2018	6.37	2.278	7.77	0.307	0.036	0.343	0.632	0.341
	24/04/2018	10.62	2.300	8.14	0.308	0.039	0.381	0.77	0.328
	23/10/2018	11.64	2.369	7.92	0.306	0.039	0.358	0.749	0.319
Northern slope boreholes	**Sampling date**		**Alkalinity**	**pH**	**Na^+**	**K^+**	**Mg^{2+}**	**Ca^{2+}**	**H_4SiO_4**
F6 63 m	27/10/2016	42.07	2.631	8.07	0.156	0.054	0.647	0.730	0.168
	22/11/2016	39.08	2.645	8.06	0.127	0.049	0.672	0.736	0.153
	09/10/2017	40.16	2.632	7.94	0.129	0.066	0.592	0.733	0.156
	09/01/2018	36.28	2.593	7.83	0.131	0.037	0.59	0.629	0.173
	25/04/2018	39.18	2.622	8.32	0.13	0.041	0.652	0.747	0.159
	23/10/2018	41.08	2.701	7.93	0.129	0.041	0.637	0.739	0.154
F7 42 m	26/10/2016	3.99	1.227	7.91	0.140	0.042	0.250	0.419	0.260
	22/11/2016	2.39	1.208	7.67	0.138	0.043	0.256	0.416	0.269
	10/10/2017	3.43	1.254	7.72	0.138	0.054	0.247	0.424	0.277
	09/01/2018	1.22	1.291	7.42	0.142	0.036	0.254	0.386	0.29
	26/04/2018	3.08	1.242	7.96	0.138	0.039	0.256	0.438	0.273
	23/10/2018	4.2	1.296	7.53	0.139	0.04	0.248	0.435	0.274
F8 27 m	26/10/2016	1.87	1.766	7.99	0.497	0.063	0.189	0.503	0.301
	22/11/2016	1.88	1.859	7.95	0.519	0.065	0.192	0.520	0.310
	09/10/2017	1.96	1.671	7.94	0.449	0.061	0.183	0.474	0.303
	09/01/2018	1.41	1.607	8	0.465	0.062	0.177	0.42	0.32
	23/10/2018	2.33	1.645	8.03	0.463	0.057	0.178	0.477	0.304

Table 3

Hydrodynamic parameters used for the reactive transport modeling of the deep water geochemical composition and mean transit time of deep water inferred in the fractured zones.

Southern slope borehole	**Fracture lengths (m)**	**Mean pore velocity (m. yr^{-1})**	**Optimized mean transit time (yr)**
F5 45 m	700	3.33	210
Northern slope boreholes	**Fracture lengths (m)**	**Mean pore velocity (m. yr^{-1})**	**Optimized mean transit time (yr)**
F6 63 m	100	1	100
F7 42 m	350	2.33	150
F8 27 m	400	0.67	597

Table 4

Geochemical fluxes and relative contributions of the shallow subsurface and deep waters to the chemical weathering in the Strengbach watershed. Calculations for the deep water are based on F5 45 m and calculations for the shallow subsurface water are based on CS1 spring (data in Ackerer et al., 2020). Geochemical fluxes are given for a unitary cross section of 1 m^2 of shallow subsurface and fractured zone in the bedrock.

		Na^+	**K^+**	**Mg^{2+}**	**Ca^{2+}**	**H_4SiO_4**	**Total**
Geochemical fluxes	**Shallow subsurface water ($kg\ yr^{-1}$)**	3.839	1.547	0.767	3.251	28.300	37.704
	Deep water ($kg\ yr^{-1}$)	0.021-0.107	0.005-0.023	0.037-0.186	0.110-0.549	0.141-0.703	0.314-1.569
Relative contribution	**Shallow subsurface water (%)**	97.3-99.4	98.6-99.7	80.5-95.4	85.5-96.7	97.6-99.5	96-99.2
	Deep water (%)	0.6-2.7	0.3-1.4	4.6-19.5	3.3-14.5	0.5-2.4	0.8-4

Table 5

Supplementary material: tables

Mineral	Chemical composition	Log (K) (25°C)
Quartz	SiO_2	-3.999
Albite	$NaAlSi_3O_8$	-20.178
K-feldspar	$KAlSi_3O_8$	-23.192
Biotite	$Si_3AlMgFe_2O_{10}(OH)_2K$	9.482
Muscovite	$Si_3Al_3O_{10}(OH)_2K$	-53.169
Anorthite	$CaAl_2Si_2O_8$	-19.488
Apatite	$Ca_5(PO_4)_3F$	-59.590
Illite	$Si_{3.5}Al_{2.1}Fe_{0.34}Mg_{0.04}O_{10}(OH)_2K_{0.6}$	-36.389

Table EA1: Chemical compositions and laboratory measured thermodynamic constants at 25°C for the different primary minerals used in this study. Data are from the KIRMAT database which is consistent with the Thermoddem database.

Mineral	Chemical composition	Kinetic constants (25°C) ($mol.m^{-2}.an^{-1}$)			α^n_{H+}		Boundary pH		Activation energy ($kJ.mol^{-1}$)
		Acid	Neutral	Basic	Acid	Basic	Acid	Basic	
Quartz[1]	SiO_2	-	3.15×10^{-6}	2.50×10^{-9}	-	-0.5	3	6	85.0[1]
Albite[2]	$NaAlSi_3O_8$	5.61×10^{-3}	5×10^{-5}	2.94×10^{-7}	0.45	-0.3	4.5	8	58.6[12]
K-feldspar[3.4]	$KAlSi_3O_8$	2.68×10^{-3}	1.02×10^{-5}	9.31×10^{-13}	0.44	-0.69	4.5	10	38.0[13]
Biotite[5.6]	$Si_3AlMgFe_2O_{10}(OH)_2K$	4.56×10^{-3}	2.39×10^{-5}	1.09×10^{-13}	0.41	-1.05	5	8	35.0[7]
Muscovite[7]	$Si_3Al_3O_{10}(OH)_2K$	1.99×10^{-5}	-	6.15×10^{-5}	0.17	-0.16	4	7	22.0[7]
Anorthite[8.9]	$CaAl_2Si_2O_8$	-	3.23×10^{-4}	-	-	-	4	8.5	40.0[14]
Apatite[10]	$Ca_5(PO_4)_3F$	5.50×10^{2}	2.96×10^{-3}	-	0.91	-	6	-	34.7[10]
Illite[11]	$Si_{3.5}Al_{2.1}Fe_{0.34}Mg_{0.04}O_{10}(OH)_2K_{0.6}$	7.92×10^{-5}	3.71×10^{-8}	3.88×10^{-14}	0.64	-0.62	5	9.5	14.0[11]

Table EA2: Kinetic constants at 25°C and activation energies of the dissolution reactions for the primary minerals used in this study. Data are from laboratory measurements and from [1] Dove (1994). [2] Chou and Wollast (1984). [3] Schweda (1989). [4] Lundström and Øhman (1990). [5] Acker and Bricker (1992). [6] Malmström and Banwart (1997). [7] Nagy (1995). [8] Amrhein and Suarez (1992). [9] Berg and Banwart (2000). [10] Guidry and Mackenzie (2003). [11] Köhler et al. (2003). [12] Blum and Stillings (1995). [13] Helgeson et al. (1984). [14] Madé (1991). The acid. neutral. and basic domains correspond to the domains where hydrolysis reactions are promoted by H^+. H_2O and OH^- respectively.

Mineral	Chemical composition	Log (K) (25°C)
K-Illite	$Si_{3.5}Al_{2.3}Mg_{0.25}O_{10}(OH)_2K_{0.6}$	-43.192
Mg-Illite	$Si_{3.43}Al_{2.24}Mg_{0.38}O_{10}(OH)_2K_{0.8}$	-38.760
Ca-Illite	$Si_{3.2}Al_{2.2}Mg_{0.1}Fe_{0.5}O_{10}(OH)_2K_{0.6}Ca_{0.15}$	-40.943
Montmorillonite	$Si_{3.83}Al_{1.84}Mg_{0.38}O_{10}(OH)_2K_{0.4}$	-35.723
Na-Montmorillonite	$Si_{3.667}Al_{2.333}O_{10}(OH)_2Na_{0.333}$	-47.951
K-Montmorillonite	$Si_{3.667}Al_{2.333}O_{10}(OH)_2K_{0.333}$	-48.191
Ca-Montmorillonite	$Si_{3.667}Al_{2.333}O_{10}(OH)_2Ca_{0.167}$	-48.101
Mg-Montmorillonite	$Si_{3.667}Al_{2.333}O_{10}(OH)_2Mg_{0.167}$	-48.201

Table EA3: Chemical compositions and laboratory measured thermodynamic constants at 25°C for the different clay solid solution end members used in this study. Data are from the KIRMAT database which is consistent with the Thermoddem database.

Mineral	Chemical composition	Dissociation equations
Quartz	SiO_2	$SiO_2 + 2H_2O \rightarrow H_4SiO_4$
Albite	$NaAlSi_3O_8$	$NaAlSi_3O_8 + 8H_2O \rightarrow Al(OH)_4^- + Na^+ + 3H_4SiO_4$
K-feldspar	$KAlSi_3O_8$	$KAlSi_3O_8 + 8H_2O \rightarrow Al(OH)_4^- + K^+ + 3H_4SiO_4$
Biotite	$Si_3AlMgFe_2O_{10}(OH)_2K$	$Si_3AlMgFe_2O_{10}(OH)_2K + 4H_2O + 6H^+ \rightarrow Al(OH)_4^- + K^+ + Mg^{2+} + 2Fe^{2+} + 3H_4SiO_4$
Muscovite	$Si_3Al_3O_{10}(OH)_2K$	$Si_3Al_3O_{10}(OH)_2K + 12H_2O \rightarrow 3Al(OH)_4^- + K^+ + 3H_4SiO_4 + 2H^+$
Anorthite	$CaAl_2Si_2O_8$	$CaAl_2Si_2O_8 + 8H_2O \rightarrow 2Al(OH)_4^- + Ca^{2+} + 2H_4SiO_4$
Apatite	$Ca_{10}(PO_4)_6F_2$	$Ca_{10}(PO_4)_6F_2 \rightarrow 10Ca^{2+} + 2F^- + 3PO_4^{3-}$

Table EA4: Chemical compositions and dissociation equations for primary minerals used in reactive-transport simulations.

References

Acker. J. G.. & Bricker. O. P. (1992). The influence of pH on biotite dissolution and alteration kinetics at low temperature. *Geochimica et Cosmochimica Acta*. *56*(8). 3073-3092.

Amrhein. C.. & Suarez. D. L. (1992). Some factors affecting the dissolution kinetics of anorthite at 25 C. *Geochimica et Cosmochimica Acta*. *56*(5). 1815-1826.

Berg. A.. & Banwart. S. A. (2000). Carbon dioxide mediated dissolution of Ca-feldspar: implications for silicate weathering. *Chemical Geology*. *163*(1). 25-42.

Blum. A. E.. & Stillings. L. L. (1995). Feldspar dissolution kinetics. *Reviews in Mineralogy and Geochemistry*. *31*(1). 291-351.

Chou. L.. & Wollast. R. (1984). Study of the weathering of albite at room temperature and pressure with a fluidized bed reactor. *Geochimica et Cosmochimica Acta*. *48*(11). 2205-2217.

Dove. P. M. (1994). The dissolution kinetics of quartz in sodium chloride solutions at 25 degrees to 300 degrees C. *American Journal of Science*. *294*(6). 665-712.

Guidry. M. W.. & Mackenzie. F. T. (2003). Experimental study of igneous and sedimentary apatite dissolution: control of pH. distance from equilibrium. and temperature on dissolution rates. *Geochimica et Cosmochimica Acta*. *67*(16). 2949-2963.

Helgeson. H. C.. Murphy. W. M.. & Aagaard. P. (1984). Thermodynamic and kinetic constraints on reaction rates among minerals and aqueous solutions. II. Rate constants. effective surface area. and the hydrolysis of feldspar. *Geochimica et Cosmochimica Acta*. *48*(12). 2405-2432.

Köhler. S. J.. Dufaud. F.. & Oelkers. E. H. (2003). An experimental study of illite dissolution kinetics as a function of pH from 1.4 to 12.4 and temperature from 5 to 50 C. *Geochimica et Cosmochimica Acta*. *67*(19). 3583-3594.

Lundström. U.. & Øhman. L. O. (1990). Dissolution of feldspars in the presence of natural. organic solutes. *Journal of Soil Science*. *41*(3). 359-369.

Madé. B. (1991). *Modélisation thermodynamique et cinétique des réactions géochimiques dans les interactions eau-roche* (Doctoral dissertation).

Malmström. M.. & Banwart. S. (1997). Biotite dissolution at 25 C: The pH dependence of dissolution rate and stoichiometry. *Geochimica et Cosmochimica Acta*. *61*(14). 2779-2799.

Murphy. W. M.. & Helgeson. H. C. (1987). Thermodynamic and kinetic constraints on reaction rates among minerals and aqueous solutions. III. Activated complexes and the pH-dependence of the rates of feldspar. pyroxene. wollastonite. and olivine hydrolysis. *Geochimica et Cosmochimica Acta*. *51*(12). 3137-3153.

Nagy. K. L.. White. A. F.. & Brantley. S. L. (1995). Chemical weathering rates of silicate minerals. *Mineralogical Society of America. Washington. DC.*

Schweda. P. (1989). Kinetics of alkali feldspar dissolution at low temperature. Ph.D. dissertation Stockholm University.